

DEFORMATION TWINNING IN MAGNESIUM USING NANO-INDENTATION

by

TINA YU-TING SU

A thesis submitted to the University of Birmingham for the degree of MASTERS OF
PHILOSOPHY

School of Metallurgy and Materials
University of Birmingham
September 2013

UNIVERSITY OF
BIRMINGHAM

University of Birmingham Research Archive

e-theses repository

This unpublished thesis/dissertation is copyright of the author and/or third parties. The intellectual property rights of the author or third parties in respect of this work are as defined by The Copyright Designs and Patents Act 1988 or as modified by any successor legislation.

Any use made of information contained in this thesis/dissertation must be in accordance with that legislation and must be properly acknowledged. Further distribution or reproduction in any format is prohibited without the permission of the copyright holder.

ABSTRACT

This study describes an investigation into nano-indentation induced deformation twinning in pure magnesium. The working objectives of this study were to clarify:

1. Whether deformation twinning is a statistical certainty
2. The positive effects of high stress on deformation twinning
3. Whether deformation twins in magnesium are strain-rate sensitive
4. The role of grain and pre-existing twin boundaries on deformation twinning
5. The efficacy of the Schmid criterion (CRSS) in predicting deformation twinning

Deformation twins induced by nano-indentation using a Berkovich tip on magnesium grains were studied using a combination of optical microscopy, SEM and electron back scattering diffraction (EBSD).

All nano-indentations made on the magnesium grains in this study induced twinning, mainly of the $\{10\bar{1}2\}$ tension twin type. The twins induced were highly reproducible in terms of twin type, size, shape, amount and orientation with respect to the indent.

Consistent with findings from other studies, deformation twins were found to react positively to increasing contact pressure. The evidence shows that twin nucleation and growth are both higher for indents made with higher stress. Moreover, deformation twins appear to be insensitive to strain-rate. Whilst pre-existing twin boundaries play no apparent role in promoting further twinning, grain boundaries twins were found to promote twinning in neighbouring grains. Finally, the twin variants formed by indenting

in different crystal orientation suggested a break-down of the Schmid criterion, hence invalidates of the CRSS evaluation for deformation twinning in magnesium. These results elucidate existing knowledge gaps in this area.

DEDICATION

I'd like to dedicate this thesis to my grandmother Mrs Yu Mei Wu-Su, and my parents Chia Jung Su and Pei Min Yang for their unreserved love and support, emotionally and financially, for my growth and development throughout the years.

ACKNOWLEDGEMENT

I would like to acknowledge Professor Ian P. Jones and Dr. Yu Lung Chiu for their academic guidance and support throughout the two years of my master's studies. Dr. Yu Lung Chiu has had significant influence on my decision to pursue postgraduate studies and has provided me the opportunity to study here at the University of Birmingham.

I'd like to also acknowledge Dr. Ming Chu, Dr. Rengen Ding, and Dr. Yina Guo for their help with navigating me through the vast sea of knowledge of crystallography and EBSD work.

I'd like to thank especially Ms. Ran Ji and Mr. Dennis Formosa for assisting me through the nano-indentation experiments, and the staff at CEM, Mr. Paul Stanley and Mrs. Theresa Morris for technical support on the SEM.

Lastly, I'd like to acknowledge the physical and emotional support from Mr. Rohan Deoganokar, and my colleagues in the EM group: Mr. Bo Pang, Ms. Xinxin Zhao, Mr. Thiago Pereira, Ms. Yu Lu and Mr. Minshi Wang.

Thank you all.

TABLE OF CONTENTS

Chapter 1. Introduction	1
1.1 Defining a deformation twin	2
1.1.1 Formal notation	2
1.1.2 Characterisation of deformation twinning	5
1.2 Material properties affected by twinning	6
1.2.1 Ductility	6
1.2.2 Strengthening effects	7
1.2.3 Fracture and deformation twinning	8
1.3 Nucleation and growth of deformation twins	8
1.3.1 Nucleation	9
1.3.1.1 Heterogeneous nucleation mechanism	10
1.3.1.2 Nucleation via elastic twinning	11
1.3.2 Physical parameters affecting twin nucleation	11
1.3.2.1 Effect of strain rate	12
1.3.2.2 Effect of temperature	13
1.3.2.3 CRSS – orientation and stress state	13
1.3.2.4 Effect of grain size	15
1.3.2.4 Nucleation sites	15
1.3.3 Growth	17
1.3.3.1 Dislocation and stress for twin growth	17
1.3.3.2 Shape of twin	19

1.3.3.3 Effect of grain size	19
1.3.3.4 Effect of orientation	20
1.4 Deformation twinning in magnesium	21
1.4.1 Magnesium	24
1.5 Final remarks and aims of this project	26
Chapter 2. Experimental procedures	27
2.1 Materials and sample preparation	27
2.2 Pre-deformation analysis	28
2.3 Nano-indentation	30
2.3.1 Experiment 1: varying stress and strain rate	32
2.3.2 Experiment 2: crystal orientation	33
2.3.3 Experiment 3: grain and twin boundaries	37
2.4 Postdeformation analysis	39
2.4.1 Mechanical response data analysis	39
2.4.2 Optical microscopic analysis	40
2.4.3 EBSD analysis	42
Chapter 3. Results	46
3.1 Reproducibility	46
3.2 Occurrence of twins	48
3.3 Effect of varying stress and strain rate	53
3.3.1 Effect of varying stress	53

3.3.2 Effect of varying strain rate	56
3.4 Twin variant selection and Schmid Factor	57
3.4.1 Indents in symmetrical direction $[11\bar{2}0]$	57
3.4.2 Variant selection for other indents	61
3.5 Effect of grain and twin boundaries	65
Chapter 4. Discussion	71
4.1 Occurrence of twins	71
4.2 Effect of varying stress and strain rate on twinning	73
4.2.1 Effect of varying stress	73
4.3 Twin variant selection and Schmid Factor	76
4.3.1 Variant selection with respect to indents in $[11\bar{2}0]$ $[2\bar{8}\bar{1}0\bar{1}5]$, $[1\bar{2}\bar{3}1]$, and $[\bar{1}3\bar{2}\bar{2}]$ directions	76
4.4 Grain boundary and twin boundary	77
4.4.1 Effect of grain boundary	77
4.4.2 Effect of twin boundary	79
Chapter 5. Conclusion	80
Reference	

LIST OF FIGURES

Figure 1	(a) Lattice structure of a $\{10\bar{1}2\}$ twin boundary and, (b) formal description of a deformation twin	3
Figure 2	Optical micrograph of twinned magnesium	5
Figure 3	Stress and strain curve of plane-strain compressed magnesium in c-axis compression and extension	7
Figure 4	Dislocation loop configuration of a stable twin nucleus	18
Figure 5	Energy evolution during dislocation dissociation and glide to produce a stable twin nucleus	19
Figure 6	The seven twinning modes in HCP metals	22
Figure 7	The relationship between twinning shear, s and the HCP axial ratio, γ	23
Figure 8	Common twinning modes in magnesium	24
Figure 9	Grain orientation map of a magnesium sample	29
Figure 10	Schematic of the Berkovich tip	31
Figure 11	Nano-indentation set up used in the current study	32
Figure 12	Proposed indent orientation for experiment 2.3.2	34, 48
Figure 13	Schematic of indent alignment	35
Figure 14	Schematic of indent alignment procedure 3 and 4 in 2.3.2	36
Figure 15	Indent positions in the grain boundary tests	38
Figure 16	Optical microscopy analysis diagram	41
Figure 17	EBSD misorientation analysis diagram	43
Figure 18	EBSD pole figure analysis diagram	45
Figure 19	Optical micrographs of six indents in $[\bar{1}2\bar{3}1]$ direction	47
Figure 20	Optical micrograph of the indent in simple direction: $[11\bar{2}0]$ - $[0001]$ - $[\bar{1}100]$	48

Figure 21	Schematic of proposed material flow under the indent	51
Figure 22	Six tension variants in magnesium with respect to loading direction $[1120]$	52
Figure 23	Optical micrographs of indents made in experiment 2.3.2	58, 59
Figure 24	EBSD analysis of indent made in $[1120]$ loading direction	60
Figure 25	EBSD analysis of indent made in $[28 \bar{1}0 \bar{1} 5]$ loading direction	62
Figure 26	EBSD analysis of indent made in $[1 2 \bar{3} 1]$ loading direction	63
Figure 27	EBSD analysis of indent made in $[\bar{1} 3 \bar{2} \bar{2}]$ loading direction	64
Figure 28	Optical micrograph of grain and twin boundaries selected for indentation	66
Figure 29	Optical micrographs of grain boundary indents	67
Figure 30	Optical micrographs of grain boundary indents	68
Figure 31	EBSD analysis of 32° -misorientation grain boundary indent	69
Figure 32	Optical micrograph of a twin boundary indent	70
Figure 33	EBSD analysis of the indent with compression twin	72

LIST OF TABLES

Table 1	Common twinning modes in FCC, BCC and HCP metals	3
Table 2	Three most common modes of twinning in magnesium	25
Table 3	Common misorientation angles in magnesium between matrix and twin	44
Table 4	Summary of the Schmid factor in [1120] direction of the six tension twin variants	53
Table 5	Stress calculation of indents made	54
Table 6	Twin number, area fraction, number density and normalised twin size of experiment 2.3.1	56
Table 7	Schmid Factor (m) and twinning frequency for sample indented in directions $[2\bar{8}\ \bar{1}0\ \bar{1}\ 5]$, $[1\ 2\ \bar{3}\ 1]$, and $[\bar{1}\ 3\ \bar{2}\ \bar{2}]$	61

CHAPTER 1. INTRODUCTION

Deformation twinning in crystalline materials is a plastic deformation mechanism that is comparable and sometimes competes with dislocation slip [1-2]. This process plays a crucial role in determining the ductility of many otherwise brittle metals [1] and creates a permanent microstructural change that affects many other material properties such as fracture toughness [3]. A majority of the research thus far has examined the nucleation [4-9] and growth process [10] alongside relevant physical parameters influencing the critical resolved shear stress (CRSS) [2, 11], growth rate [12], twin variant selection [11, 13-14] and maximum twin volume [15] in both single and polycrystalline materials. These studies present a macroscopic overview of the mechanical response, and provide the foundation for predicting material behaviour under different service conditions. Research to date has also attempted to characterise factors such as the twin nucleation site and the relationship between orientation and nucleation, but the results obtained from models are somewhat uncertain. This thesis will attempt to evaluate nano-indentation induced deformation twinning in magnesium, with the aim of characterising local mechanical responses associated with twin nucleation and growth.

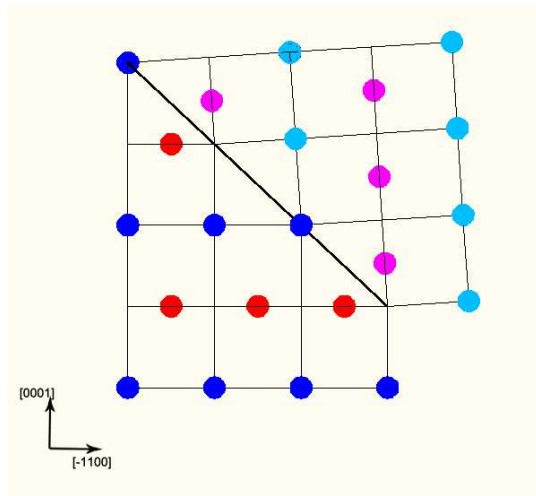
This chapter presents an overview of the nucleation and growth mechanisms of deformation twins, with reference to the various mechanical parameters known to

affect twinning events. The focus will then be narrowed down to deformation twinning, specifically in hexagonal close packed (HCP) metals, followed by a more in-depth description of twinning in magnesium.

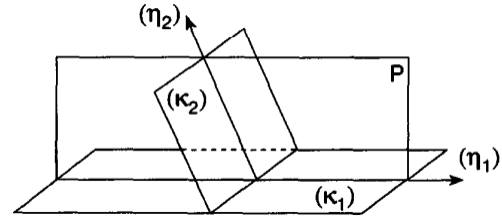
1.1 Defining a deformation twin

1.1.1 Formal notation

Microscopically, a deformation twin is a region in the crystal structure that orients differently from the crystal matrix [2]. Crystal re-orientation is a result of shearing - which is the mechanical response to stress, and subsequent shuffling at the atomic level [2, 10, 16-17]. Figure 1 is an example of a deformation twin in magnesium bounded at $\{10\bar{1}2\}$ plane to the parent crystal structure. The diagram shows also re-orientation of atoms from their original positions. A formal notation to describe the deformation twin is shown in figure 1 (b), where the twinning plane and the shearing vector are defined [2, 10]. A different set of K_1 , K_2 , η_1 and η_2 is defined for each specific twinning mode along with the magnitude of shear, s . Examples of common twinning modes in FCC, BCC and HCP metals are listed in table 1.



(a)



(b)

Figure 1. (a) lattice structure at the twin boundary of $\{10\bar{1}2\}$ twin in magnesium, (b) formal description of a deformation twin, where K_1 is the plane of shear, also known as the twin boundary, K_2 is the second undistorted plane in the twinned region, P is the plane of shear, η_1 represents the direction of shear on the K_1 plane and similarly, η_2 is the shearing direction on the K_2 plane.

	K_1	η_1	K_2	η_2	s	q
FCC	$\{111\}$	$\langle 11\bar{2} \rangle$	$\{11\bar{1}\}$	$\langle 112 \rangle$	$\frac{1}{\sqrt{2}}$	
BCC	$\{112\}$	$\langle \bar{1}\bar{1}1 \rangle$	$\{\bar{1}\bar{1}2\}$	$\langle 111 \rangle$	$\frac{1}{\sqrt{2}}$	
HCP	$\{10\bar{1}2\}$	$\langle 10\bar{1}\bar{1} \rangle$	$\{\bar{1}012\}$	$\langle \bar{1}01\bar{1} \rangle$	$\frac{\gamma^2 - 3}{3\sqrt{\gamma}}$	4

Note: γ is the axial ratio c/a for HCP metals and q refers to shuffling.

Table 1. Common twinning modes in FCC, BCC and HCP metals [2].

Since the early 1920's deformation twins have been classified as type I, II or compound [2, 10, 16]. A type I twin is where K_1 and η_2 lie on a lattice plane and lattice row respectively (rational), but K_2 and η_1 do not (irrational). Where K_2 and η_1 are

rational and their conjugates K_1 and η_2 are irrational are characteristic of a type II twin [10]. A compound twin is where all four elements are rational and is the general twinning type present in most metals [1-2, 10].

The formation of deformation twins can be accompanied by a change in physical dimension of the sample, as observed in some single crystal experiments in the 1950s [10, 18]. Clark and Craig [18] proposed that this mechanism was governed by the shear strain, ε_τ , defined by the angle between K_1 and K_2 , (2ϕ) using the equation:

$$\varepsilon_\tau = \frac{2}{\tan 2\phi} \quad (1)$$

The change in length of the twinned crystal, $\frac{l}{l_0}$, is hence given by:

$$\frac{l}{l_0} = \sqrt{1 + 2\varepsilon_\tau \sin(x) \cos(\lambda) + \varepsilon_\tau^2 \sin^2(x)} \quad (2)$$

where x is the angle between the longitudinal direction of the crystal and K_1 , and λ is the angle between the projections of the longitudinal direction on K_1 and η_1 .

1.1.2 Characterisation of deformation twinning

Metallurgical examination of a twinned metal under the optical microscope reveals lenticular or needle like micro-features of deformation twins that are usually partial or fully transgranular, as exemplified by the deformed magnesium sample in figure 2. Deformation twins can also be characterised by electron back-scattered diffraction (EBSD) [6, 13, 19], TEM [20-21], neutron diffraction [14] and x-ray diffraction [18, 22]. These four methods exploit the mis-orientation between the twinned region and the matrix to analyze twin type, size, twin volume, distribution, propagation of twinning and the evolution of twinning dislocations.

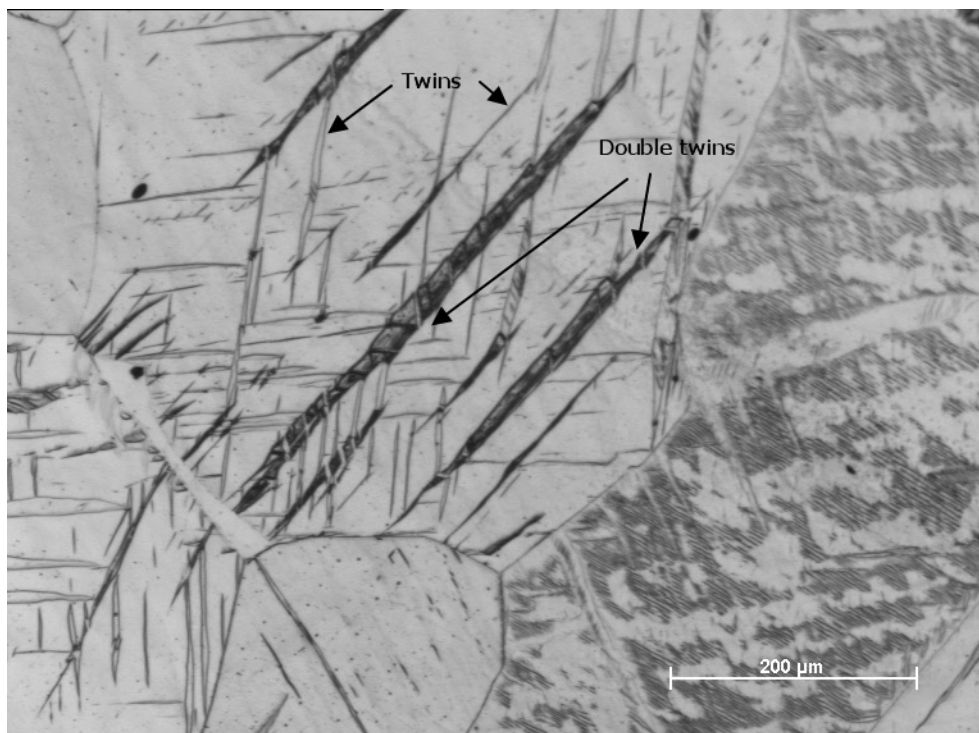


Figure 2. Deformed magnesium sample showing extensive twinning and double twinning.

1.2 Material properties affected by twinning

1.2.1 Ductility

Deformation twinning has been observed to enhance ductility [2, 8, 21]. This is a result of crystal re-orientation during twinning leading to local stress relief at the twinning site [23-24]. This means that the twinned region has a relaxed lattice compared to the matrix and is therefore a 'softer' region that can accommodate more strain. This effect is known as 'work-softening' during the initial stages of twin nucleation and growth [8, 11]. In some cases, a further contribution to ductility arises as the crystal re-orientation activates further slip or twinning systems in the twinned volume [18, 22, 24-25].

Work-softening by twinning is reflected in the characteristic sigmoidal tendency of the stress and strain curve for twinned polycrystalline samples [19, 25-27]. Figure 3 shows the true stress-strain curve of pure magnesium under plane-strain compression with characteristic curves for both slip (left) and twinning (right) [13]. Both samples were deformed close to failure and the final ductility of the twinned sample was nearly 60% greater than the slipped sample.

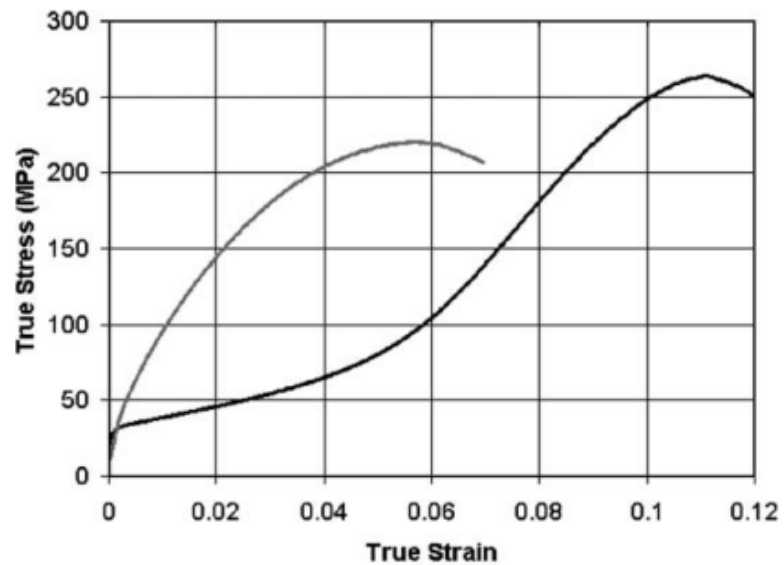


Figure 3. True stress and strain curve of plane-strain compressed pure magnesium in the c-axis compression (left) and extension (right) directions [13].

1.2.2 Strengthening effects

Deformation twinning plays a significant role in the work-hardening stage of a material as twin boundaries are effective at trapping dislocations - similar to grain boundaries [8, 25]. This phenomenon is well represented using the Hall-Petch equations by considering that the twin boundaries sub-divide a grain into smaller grains [28]. Strain hardening with deformation twins is most noticeable at the end of stage II prior to fracture [20]. In the same manner by which crystal re-orientation enhances ductility, twinning can re-orient the crystal into a 'hard' direction for further slip or twinning hence hardens the material

1.2.3 Fracture and deformation twinning

Deformation twinning can either induce or reduce fracture. Studies in the late 1920s found that cleavage crack growth in zinc is intimately associated with twin boundaries, and therefore promote fracture by cleavage crack formation. This can be rationalised by, again, the observation of crystal reorientation into a hard deformation orientation with respect to stress, leading to strain incompatibility and cleavage fracture at the twin boundary [7, 10, 23-24, 29]. It should be noted that the catastrophic mechanism of stress relief via deformation twinning resembles in many ways the process of crack formation. Yoo in 1981 stated that these two operate under similar conditions and that twinning competes with crack formation [10, 24, 30]. This is further demonstrated by Biggs and Pratt's finding that suppressing twinning in alpha iron single crystals can successfully eliminate brittle fracture [31].

1.3 Nucleation and growth of deformation twins

Deformation twinning, as suggested by its name, is a purely mechanical process [32]. Similar to slip deformation, it is driven by dislocation dissociation and movement through the crystal lattice [1, 10, 12, 33]. Yet it differs in that twinning dislocation movements cause a permanent shearing and re-orientation in the crystal lattice which can only be undone by applying force in the opposite direction [9]. How a deformation

twin nucleates and grows through a finite thickness remains the subject of investigation after many years of research [1, 12]. Following the previous section, which highlights the benefits of appropriately introducing deformation twins in a material, the following sections discuss the mechanisms behind nucleation and growth of twins along with the physical parameters known to affect each stage i.e. strain-rate, temperature, orientation, grain size, local stress state, composition, pre-strain, and interstitials/precipitates [2].

1.3.1 Nucleation

Two twin nucleation mechanisms, homogeneous and heterogeneous, have been proposed. Homogeneous nucleation involves twins nucleating from a defect-free crystal, preceded by micro-slip [2, 8, 12]. Heterogeneous nucleation, on the other hand, requires a local defect or pre-existing dislocation configuration at which high stress can be concentrated, to trigger nucleation [2, 5]. Heterogeneous nucleation is the more widely accepted model, as homogeneous nucleation requires stress levels many times higher than what is normally observed in polycrystalline or imperfect single crystal samples [34]. In the following section, the heterogeneous nucleation mechanism will be described briefly with the emphasis on HCP metals.

1.3.1.1 Heterogeneous nucleation mechanism

This section describes the heterogeneous nucleation mechanism pertaining to HCP metals. Heterogeneous nucleation begins with the gliding of Shockley partials or zonal dislocations interacting with a glissile dislocation pile-up site [2, 4, 12, 32, 35]. Shockley partials are dislocations dissociated from an elementary twinning dislocation or a slip dislocation, and zonal dislocations are defined as dislocations that shear more than one lattice plane during glide [2, 12, 34]. As applied stress is increased, the frequency of these dislocation-glides increases. Small unstable nuclei form until a simultaneous glide of multiple partials or zonal dislocations create an energetically stable twin nucleus [35]. Theoretically, both normal and zonal dislocation mechanisms can successfully nucleate stable twin nuclei and the selection is entirely dependent on the overall energy evaluation for a particular twin mode. For example, Wang *et al.* concluded that nucleation of extension twins $\{10\bar{1}2\}$ in magnesium is more energetically favourable to the zonal dislocation mechanism [35]. Twin nuclei in FCC and BCC are more likely to consist of three or more layers of low energy stacking faults [2, 34]. A stable twin nucleus takes the form of a dislocation loop that is positively dependent on dislocation pile-up and negatively dependent on twin boundary energy [34]. Twinning dislocations can only shear the crystal lattice on the designated twin plane in one stress sense along the overall twin dislocation Burgers vector - a highly direction-sensitive process [2]. If stress is applied in the opposite direction this specific deformation twin will not form.

Lattice stress relaxation upon nucleation is a direct consequence of this process. When a twin nucleus is successfully nucleated, the dislocation pile-up at the glissile site is suddenly freed and the initial twin propagation becomes self-sustained [30].

1.3.1.2 Nucleation via elastic twinning

Another rationale for heterogeneous nucleation is the formation of an elastic twin followed by a few successive dislocation glides to build a stable twin nucleus [4]. Elastic twinning is a result of large elastic strain on the matrix, yet this twin would shrink and gradually disappear once the matrix is unloaded. This theory of elastic twinning is not only of great importance to heterogeneous nucleation, but also to the shape and plastic-elastic properties of the twin tip [2].

1.3.2 Physical parameters affecting twin nucleation

Since twin nucleation is directly related to dislocation activity, physical parameters such as CRSS, temperature and grain size should be crucial in predicting nucleation conditions. However twin nucleation seems to depend on a different set of physical parameters. In the following sections, the effects of strain rate, temperature, crystal orientation, stress state and grain size on twinning will be presented.

1.3.2.1 Effect of strain rate

Deformation twinning is highly strain-rate dependent as observed in FCC, BCC and HCP metals [6, 10, 12, 31]. A simple explanation can be derived from the difference in the nature of slip and twinning. Slip requires glide of a complete Burgers vector whereas twinning is driven by smaller, more mobile partial dislocations [27, 30]. At higher strain-rates, when the material has limited response time to deform, twinning is activated in preference to slip [18]. Evidence for this can be drawn from metals such as aluminium which twins only under impact loading and not otherwise, due to its high stacking fault energy [2]. Another example is beryllium observed by Brown *et al* that when the strain rate is 1×10^{-4} /s, twinning was inactive and deformation was purely by slip. The material twinned more profusely at higher strain rates [27]. However, the relationship between twinning and strain rate is not as straightforward as one might hope. Despite Christian's summary in 1995 stating the dependency of twinning on strain rate for aluminium, iron, and copper alloys [2], recent studies have deduced rate insensitivity for deformation twinning [27, 36]. The insensitivity here is defined as there being no proportional change in twin nucleation with increase in strain rate. If, however, strain-rate is considered instead as a threshold-type parameter for twinning, then this insensitivity can be rationalised.

1.3.2.2 Effect of temperature

In 1954, Cahn suggested that the effect of temperature on twinning and slip differs in

every metal. For instance, in titanium, slip increases at higher temperatures thereby suppressing twinning, yet in magnesium, tension twins $\{10\bar{1}2\}$ were still found to be active at temperatures as high as 400°C [10]. Despite such inconsistencies, the general consensus appears to be that an increase in temperature favours slip, and hence twinning appears suppressed [18]. As far as the process of twin nucleation itself is concerned, temperature should be of very little or no importance. Temperature only appears to have an effect due to its effect on slip deformation.

1.3.2.3 CRSS – orientation and stress state

Studies by Cahn [10] of elastic twins have found twin nucleation to be associated with a stress threshold which, when surpassed, results in a spectacular development of the twin. This stress threshold for atom re-orientation is a function of lattice structure, impurities, crystal imperfections and temperature [5]. By referring to the notation used to describe slip, the threshold can be perceived as some sort of CRSS [1]. In contrast to slip, the CRSS for twinning is temperature independent [19, 37]. Surprisingly, experimental work on twinning CRSS using Schmid's law has had debatable outcomes where the scatter of the measured CRSS can be as large as 60% [1, 12, 38]. This scatter arises from the stress threshold not being a macroscopic effect but microscopic, local to each stress concentration point, thus varying with sample preparation, microstructure and composition [39].

Nevertheless, twin nucleation seems to depend, at least in part, on the Schmid criterion, as evidenced by Jiang *et al* who observed that only the grains having a high Schmid Factor were found to twin [25, 28, 40]. The Schmid Factor (SF) is a function of the applied stress and crystal orientation on a particular twinning plane. Schmid's law states [41]:

$$\tau_c = \sigma \cos \lambda \cos \alpha \quad (3)$$

where τ_c is the CRSS, σ is the applied stress, λ is the angle between the load axis and twin plane normal and α is the angle between the load axis and twinning direction. The SF, m , is the ratio between CRSS and applied stress, hence:

$$m = \cos \lambda \cos \alpha \quad (4)$$

The SF by itself is insufficient to predict the nucleation event. An internal stress state component was found to have a critical influence on twinning, when evaluated in conjunction with the SF of the variant [3, 7, 11]. For twin nucleation to occur, this internal stress state must exceed the theoretical CRSS threshold [12, 42]. A large easy basal glide stress state component would enhance twinning even for variants of lower SF, and a harder prismatic glide component would reduce the probability of

twinning for variants with a very high SF [11, 13, 23]. Again, this internal stress state was found to be temperature insensitive [8].

1.3.2.4 Effect of grain size

A Hall-Petch type relationship is generally assumed for grain size and twin nucleation. The Hall-Petch constant, k , is higher for twinning than for slip, indicating the sensitivity of twinning to grain size to be higher than that of slip [8, 15, 26, 43]. Bell and Cahn found that larger specimens of single crystal zinc twinned at lower strain than smaller specimens [12]. Further experiments have shown that grain refinement significantly suppresses twinning and that twin nucleation is therefore favoured in larger grains [10, 15, 44].

1.3.2.5 Nucleation sites

As described previously, a glissile dislocation or defect is required to accumulate the dislocation pile-up and stress concentration necessary for twin nucleation to occur. The three most probable areas in an engineering metal where this may happen are a grain boundary, pre-existing twin boundary and any impurities/precipitates.

Multiple studies on twinning have attempted to elucidate the relationship between twin nucleation and grain boundaries [8, 11, 35]. An example of this is the formation of

adjoining twin pairs (ATP) in bulk compression magnesium samples. These twins form at the same location on a twin boundary and extend into the grain [40]. Wang *et al* attempted to examine the nucleation criteria for these ATPs, including investigating the grain-grain misorientation relationship, grain size and Schmid criterion, in order to shed light on the grain boundary nucleation mechanism, but were ultimately unsuccessful [35]. From a purely physical consideration, as equation (2) clearly defines the necessary change in grain dimensions during twinning, neighbouring crystals may be pressurised and trigger twin nucleation in a polycrystalline sample. Barnett *et al.* studied the Lüders effect on extruded magnesium samples and observed grains of very low SF to have twinned under the stimulation of neighbouring twinning grains. In many instances, the stimulated grain would twin at exactly the same position on the grain boundary as its neighbouring grain's twin. This effect is found to be more pronounced for smaller grains [45]. Moreover, the study on the relationship between grain boundary misorientation and twin nucleation by Beyerlein *et. al* suggested that the average twins formed in relation to a grain boundary increases as grain boundary misorientation decreases [40]. The threshold misorientation is reported to be around 30°.

Twin boundaries are also effective dislocation barriers that may develop into a nucleation site for new or conjugate twins [24]. Geometrically, the shape of the twin tip will concentrate stress and therefore initiate further twin nucleation, similar to that of

an autocatalytic reaction [12]. Broadly speaking, twin boundaries are natural sites of high stress concentrations. The lattice distortion associated with a twin boundary during further plastic deformation could lead to fracture, recrystallisation, further twin nucleation and chemical reactivity (the preferential attacking of the grain boundary during etching) [10]. A similar rationale can be drawn for impurities and precipitates facilitating twin nucleation [18].

1.3.3 Growth

This section provides a summary of the twin growth mechanism alongside a discussion of the physical parameters which define the shape and magnitude of the resulting twin.

1.3.3.1 Dislocations and the stress for twin growth

Growth is generally considered a heterogeneous process that involves a dislocation pole mechanism, resulting in twin expansion around a dislocation 'pole' (screw dislocation threading multiple planes parallel to K_1) - similar to the operation of a Frank-Read source. Figure 4 is a schematic of a stable twin nucleus presented in the form of a dislocation loop. Under stress, the loop would expand and the matrix would

be re-oriented along the path of expansion [2].

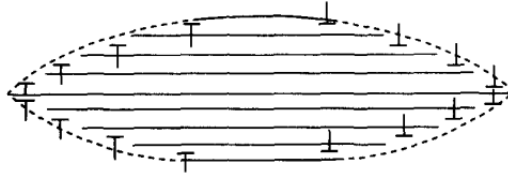


Figure 4. Schematic of the dislocation loop configuration of a stable twin nucleus [2].

This loop expansion mechanism is driven by dislocations dissociating spontaneously as they intersect with a stable twin nucleus. This interaction causes the twin to broaden, widen and sometimes induce secondary twinning [4].

Twin growth has a catastrophic nature associated with the difference in stress levels required for nucleation and growth – with growth requiring much lower energy than nucleation [8, 12]. Figure 5 from Capolungo *et al* showing the energy evolution of the twinning process to produce a stable twin nucleus [34]. The potential energy built up in the form of a stress concentration prior to nucleation is rapidly depleted during the initial catastrophic growth of the twin nucleus. Once the initial stress concentration has been exhausted, the growth process is then governed by the stress state. This is the external stress state rather than internal and its magnitude determines the maximum attainable twin volume [14, 42].

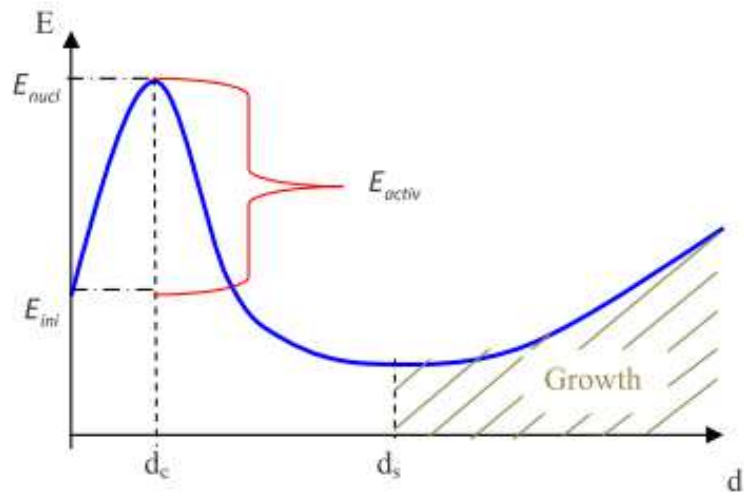


Figure 5. Energy evolution during dislocation dissociation and glide to produce a stable twin nucleus. E represents the energy and d is the size of the twin nucleus [34].

1.3.3.2 Shape of a twin

A 3-dimensional study using serial sectioning revealed that a deformation twin has a biconvex lens structure where the edge of the lens expands along the K_1 plane [10]. A matrix with a lower elastic modulus would result in a more rounded edge and a stiffer matrix would have a thinner, more needle-like twin cross-section. Twin thickening occurs in the direction normal to K_1 and the length and width expansion follow η_1 and the shear direction [5].

1.3.3.3 Effect of grain size

Similar to nucleation, the growth process is also affected by grain size. A very obvious

effect is that of limiting the maximum attainable twin size [43]. Twins, even when they consume the entire grain volume, are unable to expand beyond the existing grain boundary at room temperature.

A larger grain, however, does not necessarily equal a higher twin volume fraction. Studies show that whilst the number of twins increases with grain size, neither their thickness nor the overall twin volume changes/increases [14, 35]. This is because twinning introduces boundaries that gradually refine the grain size, and as the resulting effective grain size gets smaller, the resolved shear stress required for twin nucleation becomes higher [12]. For metals that have twin modes with low thickening ability, where twins cannot thicken to consume the entire grain, twinning saturates at lower stresses than expected [3].

1.3.3.4 Effect of orientation

The relationship between growth and crystal orientation is more straightforward than between nucleation and orientation. Twin variant selection using the Schmid Factor has a direct relationship with the final twin dimension - highly ranked grains are populated by larger and thicker twins and vice versa for lower ranked grains. [14]

1.4 Deformation twinning in magnesium

Unlike with FCC or BCC metals, HCP metals often rely on twinning to maintain general plastic flow during deformation [7, 24]. Susceptibility to twinning of HCP metals is due to the anisotropy in the thermo-elastic-plastic properties causing an intergranular distribution of internal stress states [5]. Twinning dislocations in HCP metals are nonplanar and activated upon dissociation into partial dislocations. By studying dislocation behaviour alone, one is able to explain the majority of mechanical responses observed with the onset of twinning [4]. Twinning dislocations in HCP metals also have a directional stress-sense and twin modes are triggered by either tension or compression stress on the c-axis [4, 18]. The c-axis is frequently neglected: thus ‘tension twin’ implies ‘tension along the c-axis’. Whether twinning occurs with tension or compression stress depends on the theoretical twinning shear, s , of each twin mode which is directly proportional to the axial ratio, γ , following the relationship:

$$s = \frac{\gamma^2 - 3}{3\sqrt{\gamma}} \quad (5)$$

When s is positive the twin mode is triggered by compression.

The seven possible twinning systems in HCP metals are shown in figure 6.

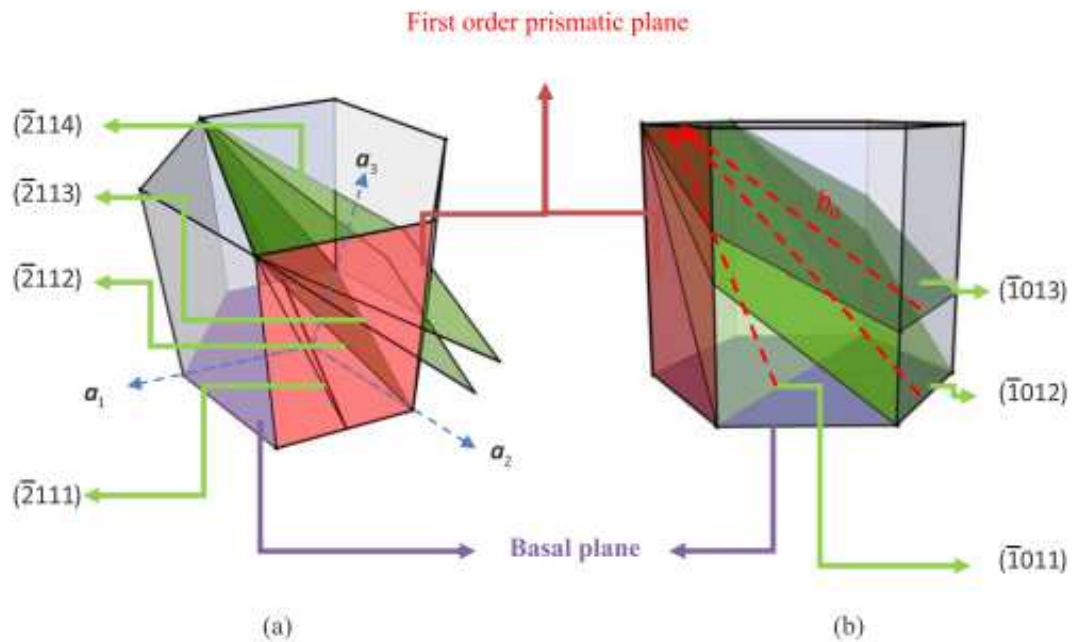


Figure 6. The seven twinning modes in HCP metals: (a) shows the $(2\bar{1}\bar{1}x)$ series and (b) shows the three $(\bar{1}01x)$ modes [34].

In 1981, Yoo examined six of the seven different twin modes available for seven engineering hcp metals and recorded their relationship with tension and compression stress on the c-axis, as shown in figure 7 [24]. This relationship alone, however, is not sufficient for predicting the twinning mode.

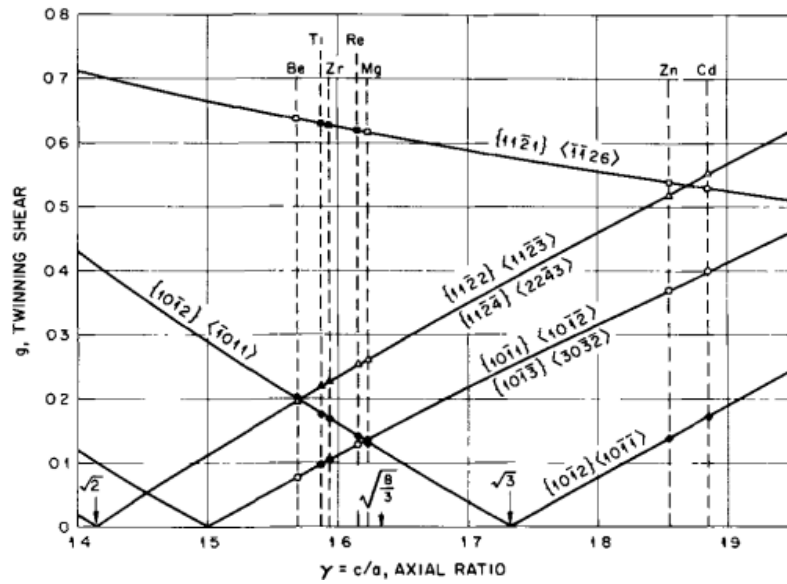


Figure 7. The relationship between twinning shear, s and the HCP axial ratio, γ . This plot is useful for predicting the twinning mode when a HCP metal is deformed in either tension or compression along the c -axis [24]

In general, ductility in an HCP metal depends on the number of available twinning modes: titanium twins in all 7 modes compared with zinc which twins only via the $\{10\bar{1}2\}$ mod [2, 24].

Deformation of HCP metals is also highly orientation sensitive [18] and shows a stronger dependence on temperature in terms of twin mode selection in comparison to FCC or BCC metals [5].

1.4.1 Magnesium

Magnesium is a relatively ductile HCP metal which deforms primarily by basal slip and twinning. Other possible deformation modes are presented in figure 8 [46]. It should be noted that double twinning $\{10\bar{1}3\} - \{10\bar{1}2\}$ and $\{10\bar{1}1\} - \{10\bar{1}2\}$ is also very common in magnesium. The nucleation of double twins is a result of activation of two twin modes of equivalent shear, shuffle and rotation occurring simultaneously in a crystal lattice [4].

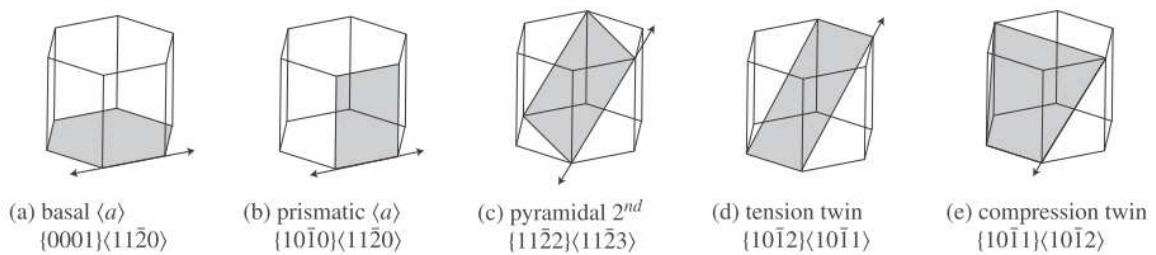


Figure 8. Common deformation modes in magnesium. Occurrence with respect to the twinning CRSS is: basal slip > tension twin > prismatic slip > compression twin > pyramidal slip [4]

Magnesium twins profusely via the $\{10\bar{1}2\}$ tension twin. Even when a magnesium crystal is oriented unfavourably, a tension twin will still develop under moderate strain rate at room temperature. Although twinning mode selection generally obeys the Schmid relationship, the selection process depends more strongly on the energy required for shearing and shuffling [2, 16]. In the case of magnesium, tension twins are preferred because of the relatively low shear and simple shuffle in comparison to compression twins. Double-twinning modes following tension twins are the preferred

deformation mechanism under dynamic deformation. [28]. The double twinning modes $\{10\bar{1}3\}$ - $\{10\bar{1}2\}$ and $\{10\bar{1}1\}$ – $\{10\bar{1}2\}$ are more energetically favourable than primary $\{10\bar{1}1\}$ and $\{10\bar{1}3\}$ compression twins. Table 2 compiles the three primary twinning modes in magnesium.

Twinning mode w.r.t. c-axis	K1	η_1	K2	η_2	s	q
Tension	$\{10\bar{1}2\}$	$\langle 10\bar{1}1 \rangle$	$\{\bar{1}012\}$	$\langle \bar{1}011 \rangle$	$\frac{\gamma^2 - 3}{\sqrt[3]{\gamma}}$	4
Compression	$\{10\bar{1}1\}$	$\langle 10\bar{1}2 \rangle$	$\{10\bar{1}3\}$	$\langle 30\bar{3}2 \rangle$	$\frac{4\gamma^2 - 9}{4\sqrt[3]{\gamma}}$	8
Compression	$\{10\bar{1}3\}$	$\langle \bar{3}032 \rangle$	$\{\bar{1}011\}$	$\langle 10\bar{1}2 \rangle$	$\frac{4\gamma^2 - 9}{4\sqrt[3]{\gamma}}$	8

Table 2. Three most common twinning modes in magnesium [2].

Tension twinning has no direct dependence on temperature and CRSS [38]. The two primary compression twin modes activate at elevated temperatures (300°C and above). It is observed, however, that secondary slip and dynamic recrystallisation of magnesium at those temperatures would limit the effect of twinning on ductility which may suggest twinning is negatively dependent on temperature [37-38, 47]. High strain rates enhance tension twinning even at high temperatures. At lower strain rates the effect of temperature enhancing non-basal slip modes overtakes tensile twinning at

high temperatures during the early stages of deformation [18-19].

1.5 Final remarks and aims of this project

Many of the works reviewed in this chapter imply that twinning is a statistical process [13-14, 27]. This means there is a distribution and a certain probability that twinning will not occur in a grain. This distribution has been attributed to the non-uniform nature of the initial metal solidification process. In order to separate the statistical nature of the data due to the starting material and from the inaccuracy of the theories and models proposed, the assumption that nucleation is a result of high local stress concentration, strain rate and crystal orientation level will be tested in the current study. Using the nano-indentation technique, a local stress concentration with certain stress, strain rate and orientation will be introduced to magnesium samples. The type (twin variant selection), number and area fraction of any deformation twins formed in relation to the conditions under which the indents are made will be examined using optical microscopy and EBSD. Nano-indentation will also be used in this study to investigate the relationship between a stress concentration and the two main twin nucleation sites proposed in the literature: grain boundaries and twin boundaries.

CHAPTER 2. EXPERIMENTAL PROCEDURES

This chapter describes the materials and methods used in this study. It begins with sample preparation, which is crucial to both nano-indentation and EBSD. The procedure for pre-deformation analysis is then presented. This is followed by a detailed description of the three nano-indentation experiments designed to examine the effects of four physical parameters, including the post-deformation analysis.

2.1 Materials and sample preparation

Vacuum cast commercial purity magnesium (99.95%) was employed in this study. Samples were machined from the cast using a power saw and then cut into 5~10 mm slices using an electrical discharge machine (EDM). The slices were annealed in an Elite BSF 12/10-2416-2116 furnace at 300°C for two hours followed by air-cooling to remove any residual strain in the material. This was followed by the normal metallurgical procedures of grinding and polishing: first using 400, 800, 1200 and 4000 grade SiC paper and then 1 μ m diamond solution on a Struers NAP MD polishing disc on a mechanical wheel. A chemical polishing solution consisting of 80% ethanol and 20% nitric acid (70% nitric acid 30% H₂O) was used between the 4000 grade sand paper and the final polishing stage, immersing the sample in the solution

for 30 seconds. This process not only reduces the time in the polishing stages but also removes the surface residual strains introduced during the grinding. After the 1µm diamond polish the samples were again immersed in the chemical polish for three seconds to remove the surface residual strain and reveal the grain boundaries.

Magnesium oxidises readily in normal atmosphere; the samples were therefore prepared immediately before each nano-indentation test followed shortly after by optical analysis and EBSD. The samples were stored in a desiccator in between tests and analysis. Once a sample had been exposed to the atmosphere for more than three days a gentle mechanical polish was applied to remove any oxide formed using 1µm diamond on a Struers NAP MD disc, followed by immersion in the chemical polish for 3 seconds prior to further EBSD analysis.

2.2 Pre-deformation analysis

Pre-deformation characterisation of the samples included optical microscopy and grain orientation mapping using EBSD. Optical imaging provided a map of the sample surface for locating suitably sized grains, while EBSD provided crystal orientation and grain boundary information for identifying grains with the desired orientation for indentation.

An optical image collage was produced from each sample using the Axiovision 40 software from Carl Zeiss Imaging Solutions on a Zeiss Axiotop2 optical microscope. Crystal orientation was measured using the Channel 5 software package from Oxford Instruments using a Nordly's detector in a Philips XL-30 SEM. The crystal orientations and grain boundary angles for each grain were measured using the EBSD and then marked on the optical image collage. Figure 9 is an example of the final grain orientation map used during nano-indentation.

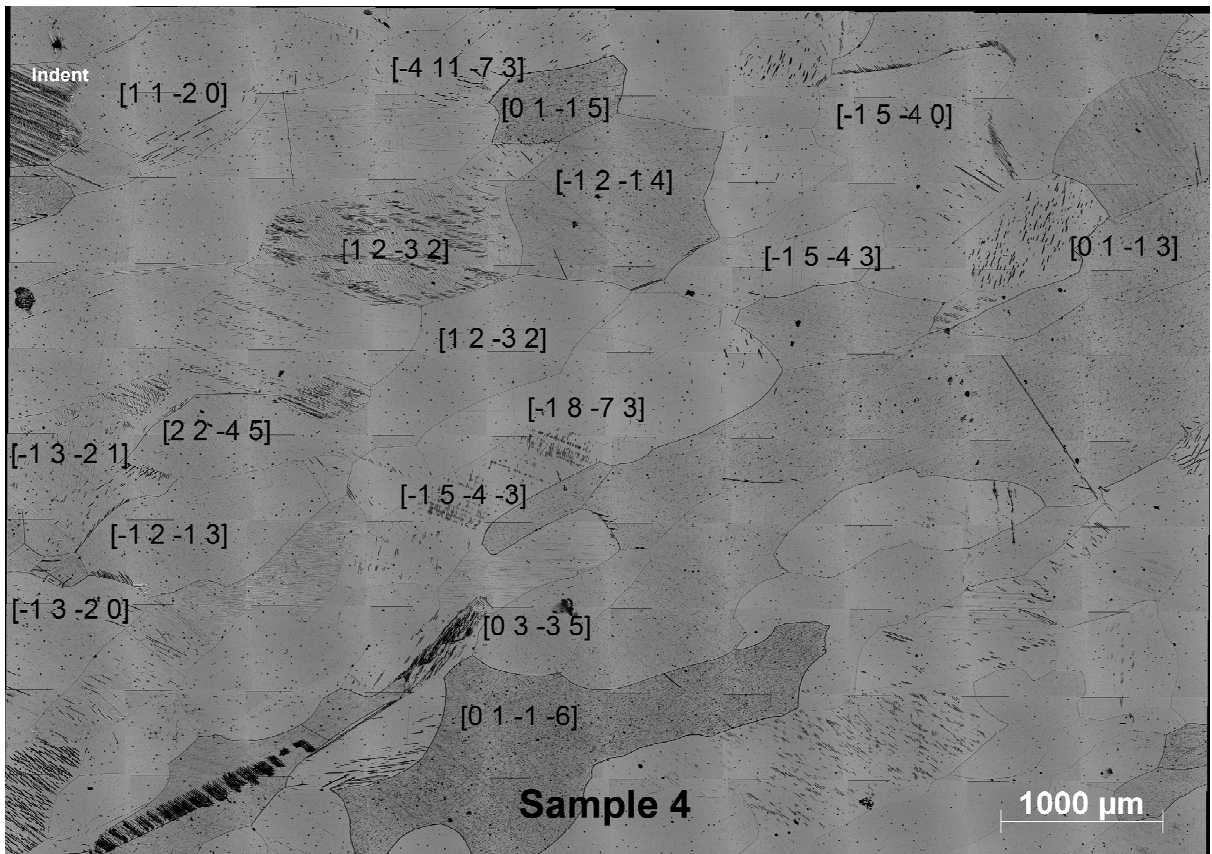


Figure 9. Grain orientation map of sample 4. The normal directions for some grains are labelled on the image.

2.3 Nano-indentation

Three indentation tests have been designed to study the effects on twinning of –

- 1) varying stress and strain rate (section 2.3.1);
- 2) crystal orientation (section 2.3.2);
- 3) the relationship between twin nucleation and grain/twin boundaries (section 2.3.3).

A Nano-test 600 nano-indentation apparatus with a Berkovich tip (figure 10) was employed. The indenter tip was fitted on a vertical pendulum controlled by a set of capacitor plates with a functional load range between 1 and 500 mN and a loading rate range between 0.1 and 100 mN/s. The sample was mounted onto a cylindrical sample holder using a small amount of superglue and was then loaded onto the sample stage as shown in figure 11. Once the sample was loaded, it was first brought to the optical microscope section of the apparatus for alignment. Cross-hair calibration was then conducted prior to each set of tests to ensure the indents fall exactly on the programmed positions. When the indentation set up was aligned and calibrated, the sample was moved to the desired location on the sample surface with reference to the grain-map taken with the optical microscope. Indentation parameters including position, maximum load and loading rate for each set of tests were then input into a controlling computer programme. The indents were positioned carefully apart (about 10 times the size of the largest indent) to prevent the interference

between neighbouring indents. All the tests described in the following sections were load-controlled with a prescribed constant loading rate and a dwell time of 20s. Once the apparatus was set and programmed, the sample was then brought back to the indentation section of the apparatus and scheduled to run, usually overnight, when the environment was more stable.

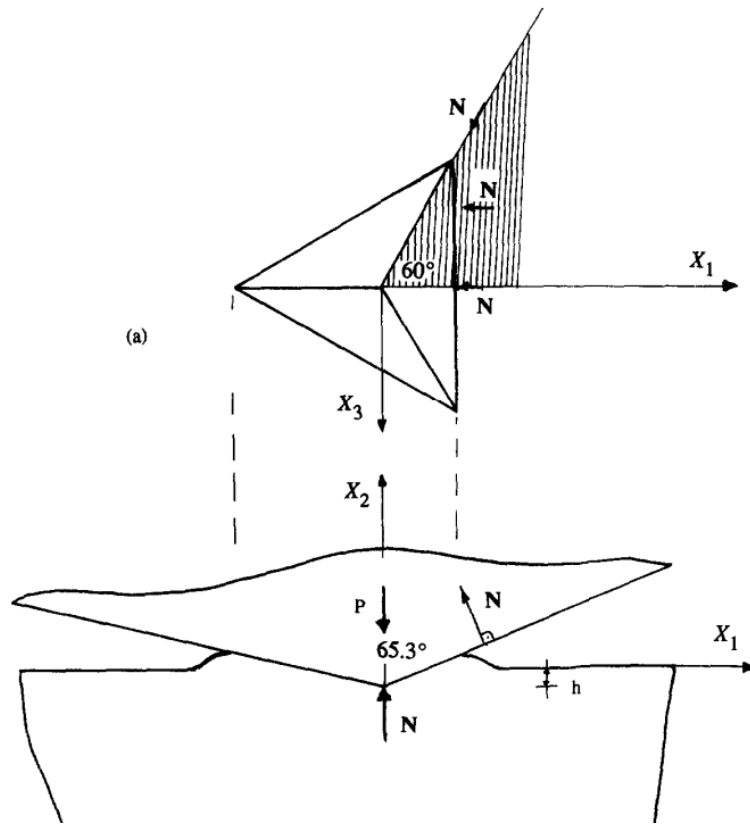


Figure 10. Schematic of the Berkovich tip, (a) top view, (b) side view [48]

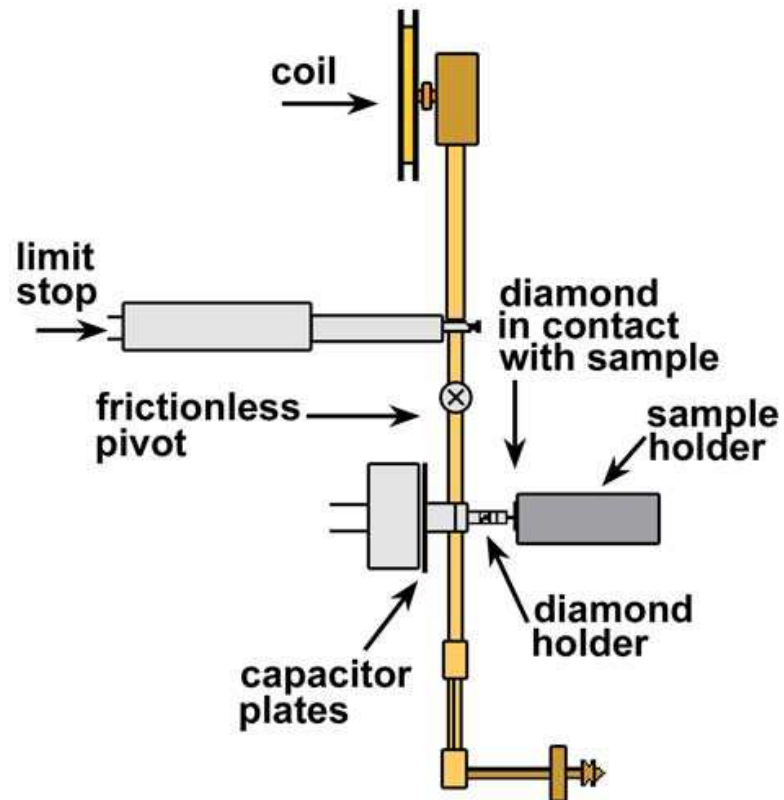


Figure 11. The nano-indentation set up used in the study [49]

2.3.1 Experiment 1: varying stress and strain rate

The nature of nano-indentation prevents the direct measurement of overall strain induced during indentation, as indentation causes a strain-gradient in the volume surrounding the indent. An alternative approach is to use the following definition of indentation strain rate ($\dot{\epsilon}$):

$$\dot{\epsilon} \propto \frac{\dot{\Delta}l}{l_0} \propto \frac{\dot{P}}{P_{\max}} \quad (6)$$

where Δl is the change in dimension due to deformation, l_0 is the original dimension

of the sample, \dot{P} is the loading rate and P_{\max} is the maximum load applied. It hence becomes possible to examine the effect of strain rate on twinning by varying the loading rate while keeping the maximum load constant. Three loading rates over two orders of magnitude: 0.1, 1 and 10 mN/s were used in this study.

Two maximum loads, 50 and 200 mN, were used to examine the effect of maximum stress on twinning. Taking advantage of the indentation size effect phenomenon, wherein indentation hardness increases with decreasing indentation depth due to strain-gradient plasticity associated with the storage of geometrically necessary dislocations [50-51], the volume under the 50 mN indent is expected to experience a higher maximum mean stress than that under the 200 mN indent.

Each set of loading rate and maximum load was repeated to ensure that the twins produced are reproducible for each test condition.

2.3.2 Experiment 2: crystal orientation

The relationship between the twin variant selection and the Schmid Factor was examined by indenting the sample along a simple direction. Crystal orientation (sample normal direction) mapping using EBSD effectively located grains with a normal direction of $[11\bar{2}0]$ to indent (figure 9). By marking a straight line on the sample

near the targeted grain using a blade it was possible to orient the triangular Berkovich indent symmetrically along the $[11\bar{2}0]$, $[0001]$ and $[\bar{1}100]$ orthogonal system, as shown in figure 12. The orienting procedure was as follows:

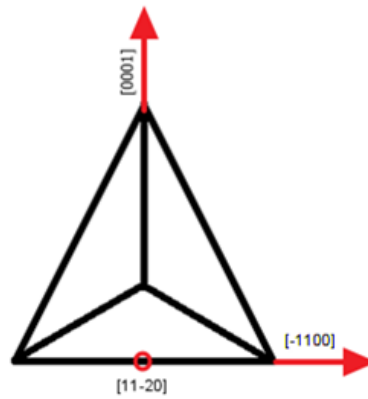


Figure 12. Proposed indent orientation for experiment 2.3.2

1. An SEM image was first taken near the blade mark and the target grain. A Kikuchi diffraction pattern obtained from the target grain was then obtained using the Flamenco EBSD software. By piecing the two together, the following figure was constructed:

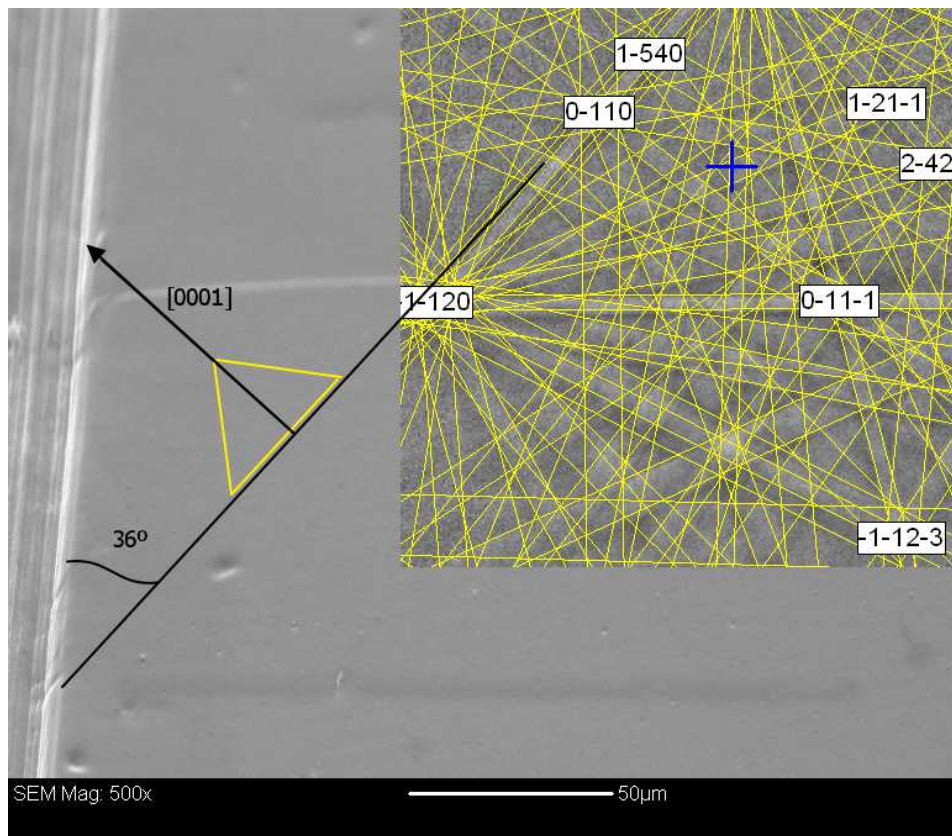


Figure 13. Schematic showing the relationship between the proposed triangular indent orientation (in yellow) and the blade mark (striations on the left). The Kikuchi diffraction pattern on the right was used to identify the [0001] direction which becomes the axis of the triangular indent.

The yellow triangle shows the desired indent orientation with regard to the blade mark: the base line of the triangular indent is parallel to $[\bar{1}100]$ and at 36° to the edge of the blade mark, and a triangle symmetry axis lay along the [0001] direction of the target grain.

2. An indent was made near the blade mark to establish the orientation of the indenter tip.

3. Under the nano-indenter's optical microscope, the indenter tip orientation (base and the symmetry axis) was examined and labelled on the microscope monitor, as shown in figure 13 (a).

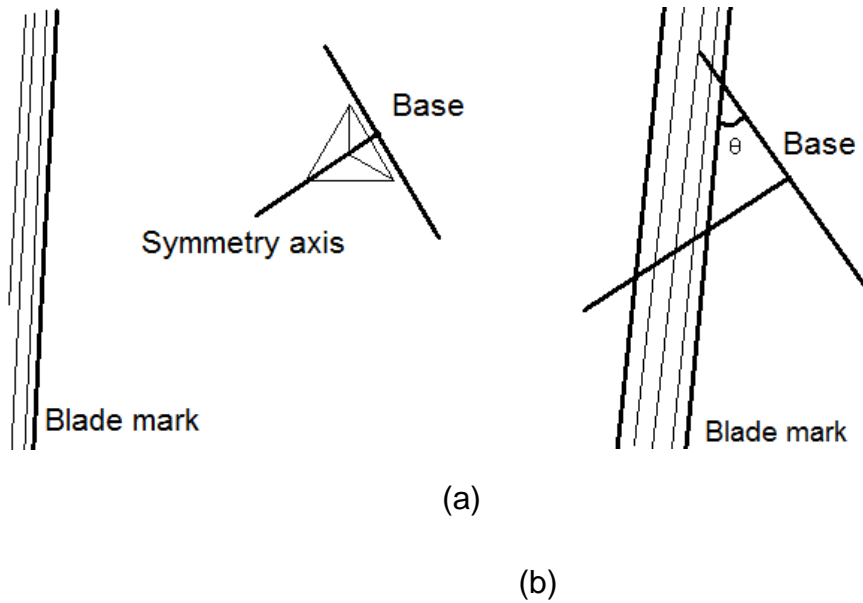


Figure 14. Schematic showing steps 3 and 4 of the orienting procedure. The triangular indent in (a) represents the indent made in step 2.

4. The sample was then moved so that the blade mark intersects with the indent orientation marked on the microscope monitor. The angle between the blade mark and the base-line of the indent was measured by a protractor (figure 14 (b)).

5. By calculating the difference between the angle measured in step 1 and 4, the sample rotation angle was obtained. The sample holder was then loosened and

rotated until the base of the indent sits perfectly at 36° to the blade mark.

6. Once the sample is aligned, three indents were made at 200mN with a loading rate of 1mN/s. These are labelled 00, representing indents at 0° rotation with respect to the direction specified in figure 13.

The stress distribution underneath an indent is known to be complex [52], and it is uncertain how the different stresses will affect twin nucleation and growth. To examine how the indent geometry, and thus stress under the indent influences twinning, the sample is rotated so that the three triangular sides of the Berkovich indent contact the sample at different angles from the first orientation (with respect to the crystal). Two more sets of indents were hence made on the same grain by rotating the sample, using steps 4 and 5, by 45° and then another 45° clockwise labelled '45' and '90' respectively. The overall loading direction, which is along the sample normal direction, and indentation parameters were kept the same.

2.3.3 Experiment 3: grain and twin boundaries

Using EBSD, several grain boundary misorientation angles were labelled on an optical micrograph collage of the sample surface. The three grain boundaries selected for indentation had grain boundary misorientation angles of 14° , 32° and 80°

respectively. An indent was made directly on each of the grain boundaries and then a set of three indents was made across, but not directly on the grain boundary, as shown in figure 15. The distance between the indent closest to the grain boundary and the grain boundary (T2) was kept to under $60\ \mu\text{m}$ (average indent size is around $20\ \mu\text{m}$ and the effective plastic volume is generally said to be around three times the indent size).

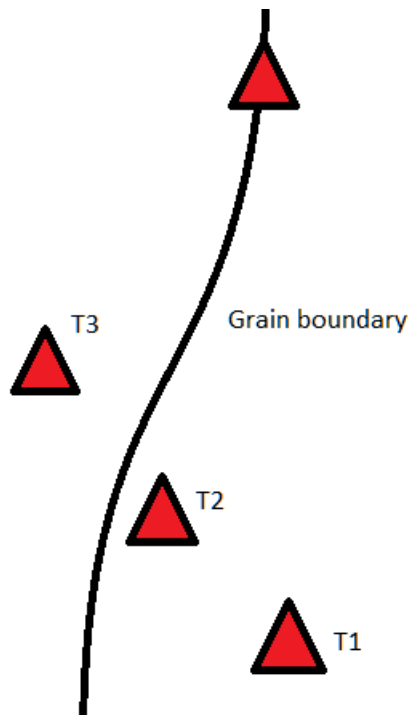


Figure 15. Indent positions in the grain boundary tests.

Similar tests were conducted across an annealed pre-existing twin, so that one indent falls on top of the twin boundary and three are across the twin. These indents were made with a maximum load of $200\ \text{mN}$ and a loading rate of $1\ \text{mN/s}$.

2.4 Post- deformation analysis

Indent analysis methods post deformation are described in the following section in three parts – first, analysis of the indentation test data, followed by optical microscopy and lastly EBSD.

2.4.1 Mechanical response data analysis

Results from the above three experiments were output directly as load versus depth data that can be extracted from the nano-indentation computer in the .ind format. Pyramidal analysis, which corrects the data for the indenter tip geometry and the machine's calibration, was conducted for all the data collected using the Nano-test Platform 3 software in 'analysis' mode. The data points can then be accessed and exported in a .txt format using the 'review data file' function. A numerical zero-correction, for the non-zero starting depth the machine sometimes records, was then carried out using a correction calculation spreadsheet obtained from users in charge of the nano-indentation apparatus in the Surface Group (under Professor H. Dong) at the University of Birmingham (Appendix). This includes inputting the starting depth of each test and the corresponding test data. The spreadsheet computes contact depth (h_c), projected area (A_p), and other parameters which are not used in this study such as hardness (H), and elastic modulus (E_r) for each of the tests. The

projected area is used in conjunction with the twin area measured using the optical microscopic image analysis method to calculate twin area fraction for each indent.

The contact area of each indent (A_c) was calculated using the following equation [48]:

$$A_c = \frac{A_p}{\cos(24.7^\circ)} \quad (7)$$

where the 24.7° corresponds to the angle between the Berkovich indenter planes with a flat sample surface, as shown in figure 10.

The stresses underneath an indent are complex and difficult to calculate. However for the purposes of this study, a simplified calculation based on the averaged stress under the indent has been employed using A_c and P_{max} . Hence the highest stress achieved during each indent test is calculated using the following equation:

$$\sigma = \frac{P_{max}}{A_c} \quad (8)$$

2.4.2 Optical microscopic analysis

Once the samples were extracted from the nano-indentation apparatus, optical micrographs were taken to observe the indents made. If any twins had formed from an indent, the twinned area was then measured using the image analysis function in

the Axiovision 40 software. By setting the programme up so that it brings out a good contrast between the twins and the surrounding matrix, it was possible to isolate and select the twinned area as 'phase 1'. Under the 'Interactive Processing of the Measurement Mask' tab, any twins omitted by the previous stages can be added using the 'Add objects' function with a 'curved' line setting. Once all of the twins are selected, the 'Draw separation lines' function was used to eliminate the twin area inside the indent area by drawing a triangle connecting the three corners of the triangular indent. An example of the results from this process is displayed in figure 16.

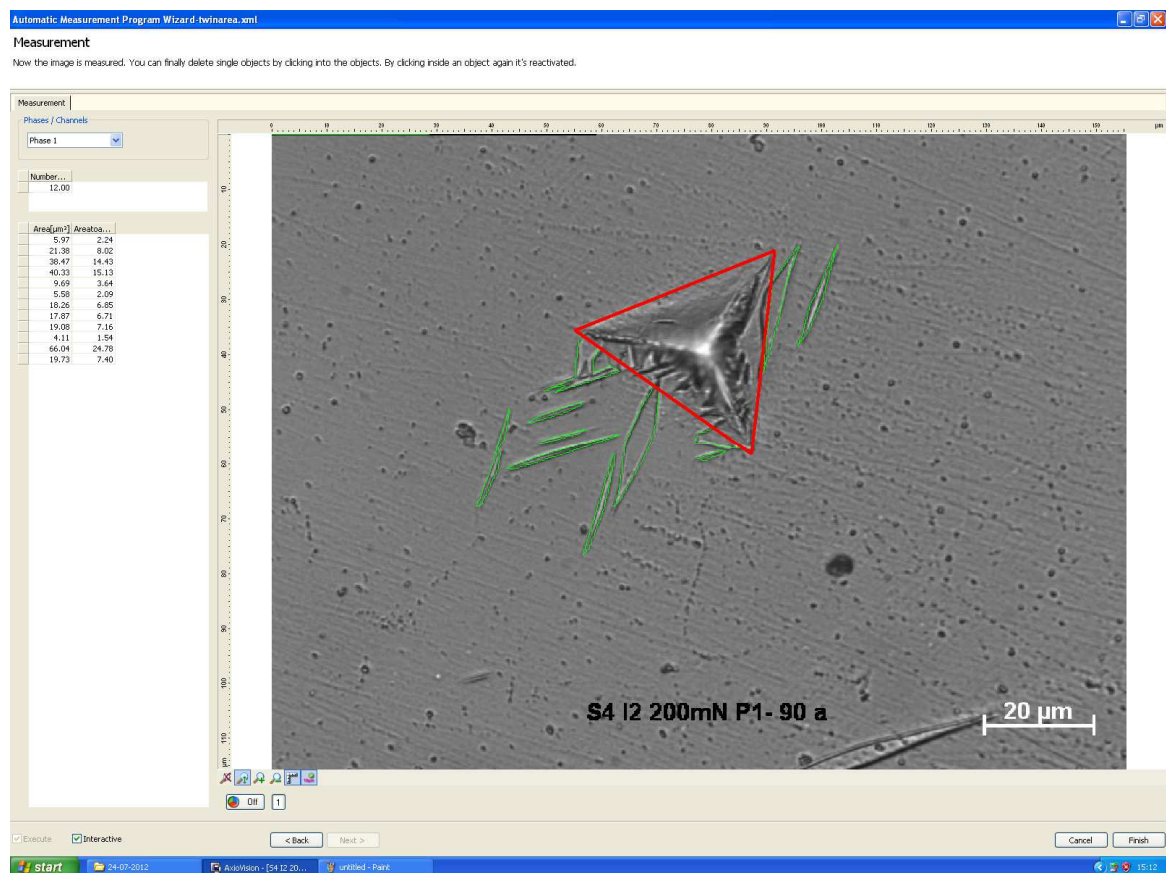


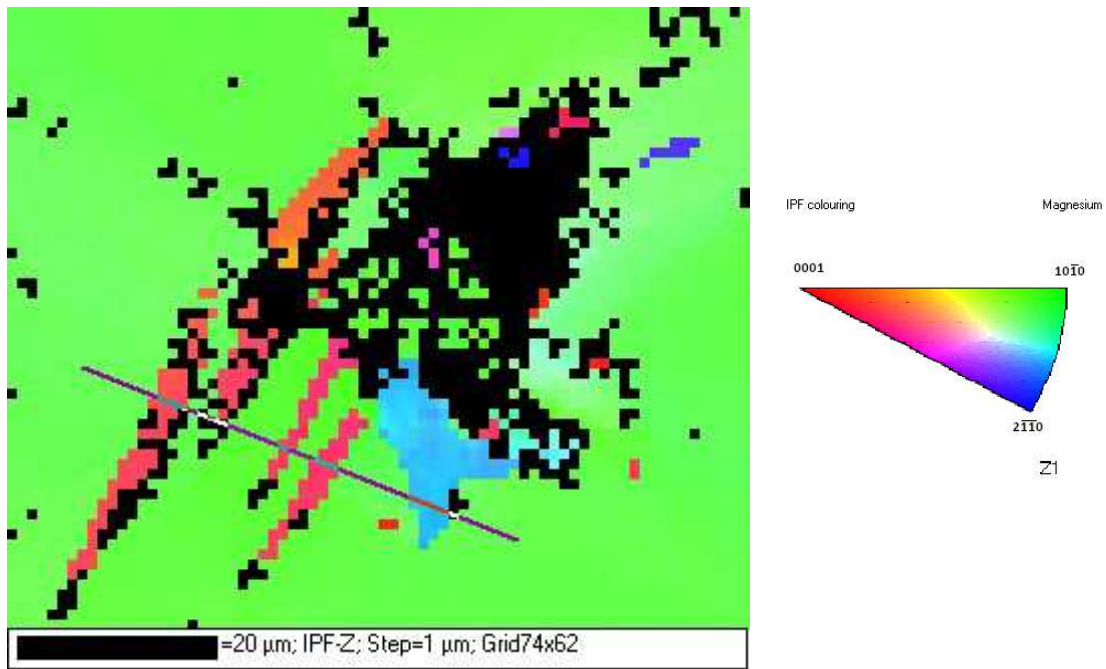
Figure 16. An example of the optical microscopic image analysis to measure most of the total twinned area (in green). The red triangle represents the indent area, or in other words the projected area, A_p , of the indent.

The image analysis software outputs the area of the selected phases (i.e. twins formed). This information is then used to calculate the area of the twins formed relative to the projected area of the indent obtained in the previous section.

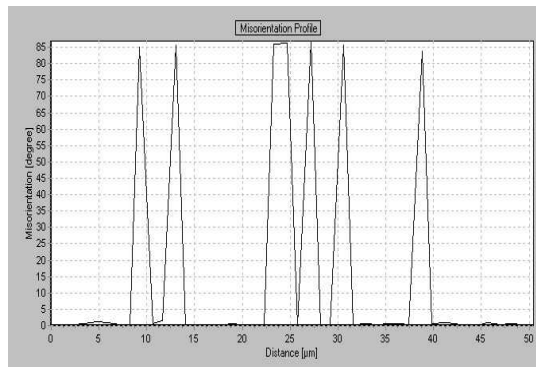
2.4.3 EBSD analysis

EBSD using Flamenco in the Channel 5 package was employed to examine the type and variant of the twins formed from the nano-indentation tests. In each scan, an area was selected from the sample surface that covers the indent and twins. Depending on the indent size and the spread of the twins, magnifications of 500x, 1000x and 2000x were used with step sizes (pixel size) of 2 microns, 1micron and 0.5 microns respectively.

Twin type is determined by measuring the misorientation angle between the matrix and twin across the twin boundary, as shown in figure 17. Then using the characteristic misorientation angles of the most common twin types in magnesium in table 3 [13], the twin type can easily be identified.



(a)



(b)

Figure 17- Misorientation angle measurement using the Tango software in the Channel 5 package by Oxford Instruments. (a) EBSD scan of an indent in sample 4 in IPF-colouring. All pixels in green represent matrix and pixels in blue, orange/pink are the twins formed from the indentation. The crystal misorientation profile (b) is computed using the misorientation tool in the Tango package, where a line is drawn across four twins, as seen in the lower half of (a), and the misorientations between each pair of pixels are evaluated and displayed along the length of the line.

Type of twin	Misorientation angle/axis
$\{10\bar{1}1\}$	$56^\circ \langle 1\bar{2}10 \rangle$
$\{10\bar{1}2\}$	$86^\circ \langle 1\bar{2}10 \rangle$
$\{10\bar{1}3\}$	$64^\circ \langle 1\bar{2}10 \rangle$
$\{10\bar{1}1\}-\{10\bar{1}2\}$	$38^\circ \langle 1\bar{2}10 \rangle$
$\{10\bar{1}3\}-\{10\bar{1}2\}$	$22^\circ \langle 1\bar{2}10 \rangle$

Table 3, Misorientations between matrix and commonly occurring twins in magnesium [13]

For each twin type, there are six variants (36 for double twins). In order to verify whether the appearance of a twin variant is related to the magnitude of its Schmid Factor, each twin variant formed in the crystal-orientation indentation test was identified using the following method. If a tension twin is identified in the previous step, using the Mambo software in the Channel 5 package a $\{10\bar{1}2\}$ pole figure is constructed, as shown in figure 18 (same indent EBSD scan as figure 16). Then by calculating the angular relationship between each of the 6 variants and the x, y, z directions of the matrix, the 6 variants can be labelled. Since the matrix shares the same K1 plane as the twin, a pixel in the twinned area and anyone in the matrix would share the same position on the pole figure, and therefore identify the twin variant. The twin represented by the colour pink/orange in figure 17 (a) is the $(0\bar{1}12)$ and blue is the $(01\bar{1}2)$ variant.

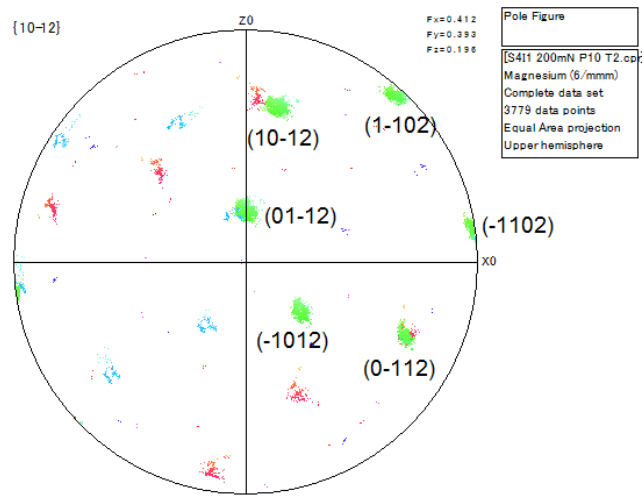


Figure 18. Pole figure of the $\{10\bar{1}2\}$ family of planes with all six variants labelled. The different colours correspond to the colouring on figure 17 (a).

CHAPTER 3. RESULTS

Optical microscopy revealed the formation of deformation twins around all indents. EBSD scans confirmed the existence of tension twins in all samples, with several occurrences of double twinning $\{10\bar{1}2\} - \{10\bar{1}2\}$ via intersection [13, 24, 53] and one instance of compression twinning $\{10\bar{1}1\}$.

3.1 Reproducibility

To measure the reproducibility of indentation induced twinning in magnesium we examined indents repeated under three different loading conditions. Optical micrographs on the left hand side in figure 19 are very similar to the three on the right hand side. This indicates that indents made with the same physical parameters are highly reproducible.

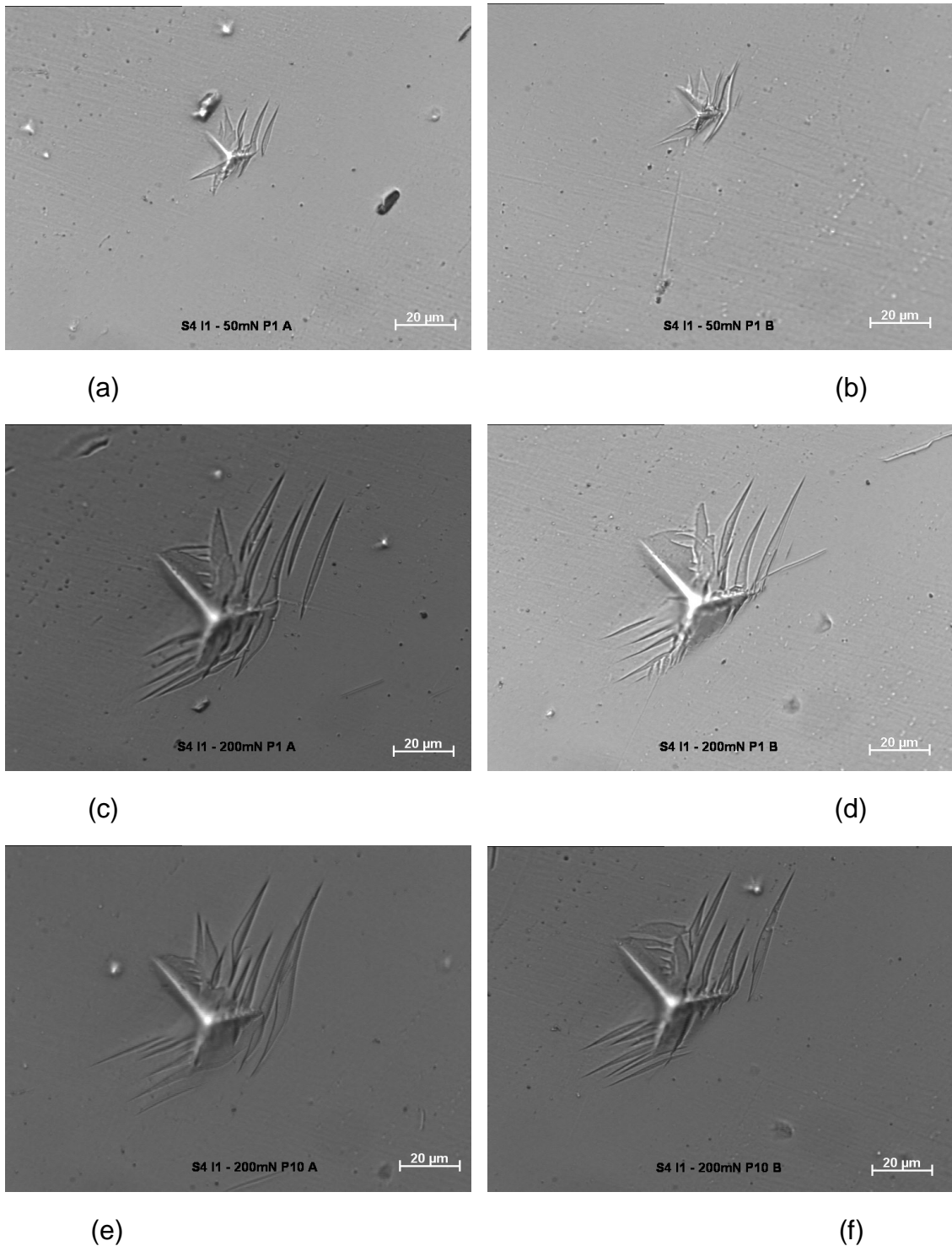


Figure 19. Optical micrographs of six indents made in three different loading conditions on grain with sample normal $[\bar{1}\bar{2}\bar{3}1]$: (a) and (b) with loading rate of 1 mN/s and a maximum load of 50 mN, (c) and (d) with loading rate of 1 mN/s and maximum load of 200 mN and (e) and (f) with load rate of 10 mN/s and maximum load of 200 mN.

3.2 Occurrence of twins

The response of pure magnesium to indentation and the subsequent twin nucleation and growth are described in this section. Figure 20 is an optical micrograph of the indent along the simple direction $[11\bar{2}0]$ described in section 2.3.2 (figure 12 reproduced here). EBSD identified the twins formed around the indent to be of the four variants labelled in figure 20: $(\bar{1}012)$ in pink, $(10\bar{1}2)$ in red, $(0\bar{1}12)$ in light blue and $(01\bar{1}2)$ in yellow.

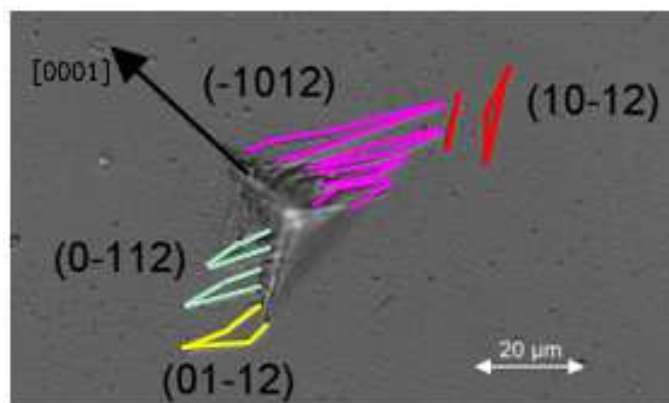


Figure 20. Optical micrograph of the indent in simple direction: $[11\bar{2}0]$ - $[0001]$ - $[\bar{1}100]$ with twins formed due to indentation highlighted in four colours representing four different tension twin variants: $(\bar{1}012)$ in pink, $(10\bar{1}2)$ in red, $(0\bar{1}12)$ in light blue and $(01\bar{1}2)$ in yellow.

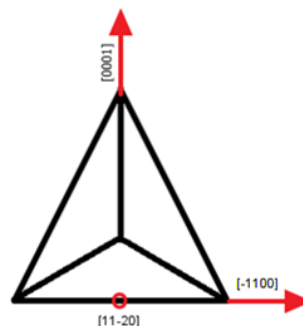


Figure 12. Reproduction of indent orientation in simple direction $[11\bar{2}0]$

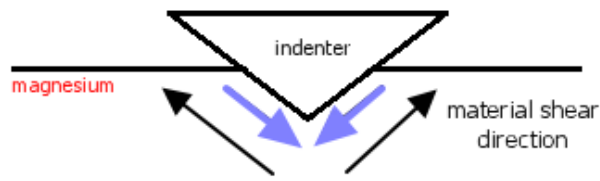
The twins are formed in response to the stress applied on the magnesium underneath the indent. The material flow under a Berkovich indent is shown in figure 21. When the indent pushes into the magnesium, material immediately next to the indenter moves down along the indenting direction as shown by the blue arrow in figure 21 (a). Magnesium twins in response to this shear. As stress builds up underneath the indent and the material relieves this by flowing towards the strain-free surroundings in the radial directions – some material re-surfaces a distance away from the initial indent site, causing the further twinning by different modes.

Although the stress-strain field underneath a Berkovich indenter is often complicated [59], it is attempted here to understand the material response to the applied stress using a simplified Schmid factor considerations.

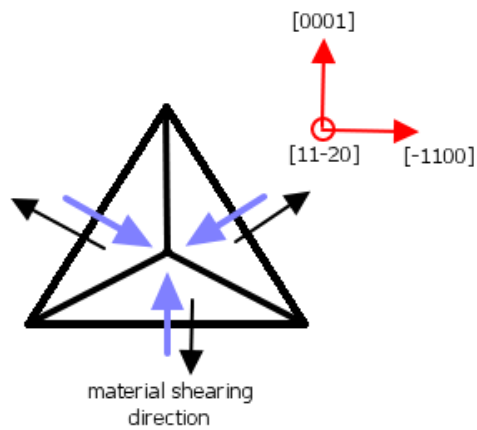
Let's first consider the relationship between the six tension twin variants, which appeared in all indent tests, illustrated in figure 22, and the material shear described in figure 21 (c). First it must be noted that the shear planes of variants $(1\bar{1}02)$ and $(\bar{1}102)$ are parallel to the loading direction $[1120]$ and the associated shear can therefore make no contribution to the volume immediately under the indent tip illustrated in figure 21, and thus the two systems are inactive here. Given that twinning is a direction sensitive process, each twin variant will operate only when shear follows the η_1 direction (see figure 22). Hence at initial contact, the shears on

the left and right sides of the indent (in figure 21 (a) and (b)) would initiate the $(0\bar{1}12)$ and $(\bar{1}012)$ twins. Notice here the direction of material moving down with the right and left side of the indent matches the direction shown in figures 22 (a) and (b). Material shear on the third side (III) of the indent will not trigger any twin since the shear direction contributes to none of the all four tension twin variants discussed here. As material re-surfaces, twin variants $(01\bar{1}2)$ and $(10\bar{1}2)$ would form further away from the indent on the left and right sides. Again the twinning directions in figures 22 (c) and (d) match the direction of material movement shown in figures 21 (b) and 21 (c). This explains the twins shown in figure 18.

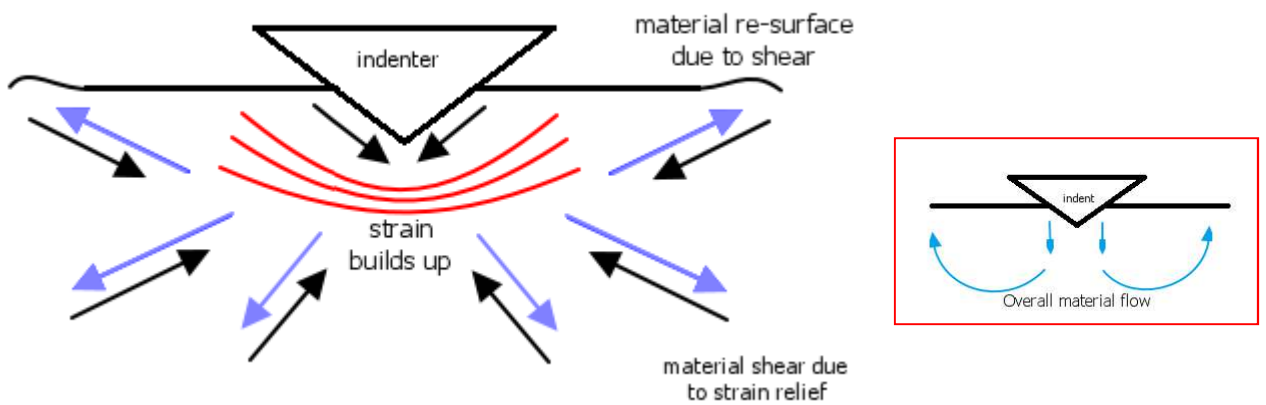
Table 4 summarises the Schmid Factors calculated for all six tension twin variants and the twin occurrence with respect to the triangular indent in figure 19.



(a)



(b)



(c)

Figure 21. Material flow underneath the indenter: (a) material flow at initial contact in profile view, (b) material flow at initial contact from bird's eye view, (c) material response to strain build-up as indentation progresses.

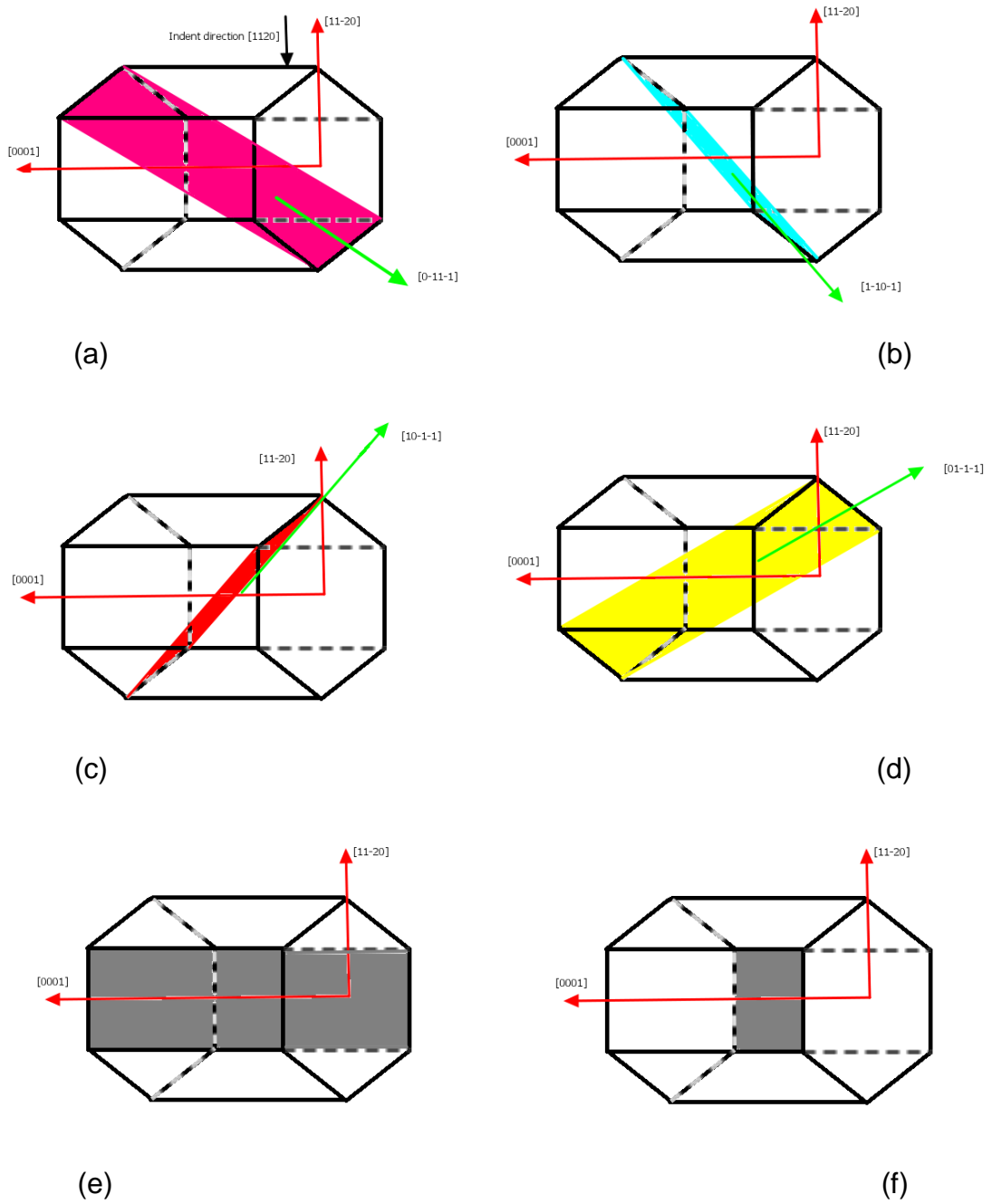


Figure 22. Six tension variants and their twin shearing directions (green arrow): (a) $(\bar{1}0\bar{1}2)$ includes indent direction $[1120]$, (b) $(0\bar{1}\bar{1}2)$, (c) $(10\bar{1}2)$, (d) $(01\bar{1}2)$, (e) $(1\bar{1}02)$ and (f) $(\bar{1}\bar{1}102)$.

Tension twin variants		$(10\bar{1}2)$	$(01\bar{1}2)$	$(\bar{1}012)$	$(0\bar{1}12)$	$(1\bar{1}02)$	$(\bar{1}\bar{1}02)$
Schmid Factor [1120]		0.374	0.374	0.374	0.374	0	0
Sides of triangle	Right	Far	-	Immediate	-	-	-
	Left	-	Far	-	Immediate	-	-
	Bottom	-	-	-	-	-	-

Table 4. Summary of the Schmid factor in [1120] direction of the six tension twin variants and the twins formed as a result of the triangular indentation in the $[11\bar{2}0]$ direction and with the orientation shown. The Schmid factors were calculated using the loading direction [1120], twinning plane normal direction following K1, and slip direction following η_1 of each variant.

3.3 Effect of varying stress and strain rate

3.3.1 Effect of varying stress

In experiment 1 (c.f. section 2.3.1), six indents each were made with maximum loads of 50 mN and 200 mN to examine the effect on twinning of varying stresses under the indent. Affirming to the indentation size effect phenomenon, the calculated mean stress immediately underneath the 50 mN indents was higher than that under the 200 mN ones. The average values shown in table 5 are 329.3 MPa and 264.9 MPa respectively.

	Mean stress (MPa)	Standard Deviation (MPa)
<i>50 mN indents</i>	329.3	31.3
<i>200 mN indents</i>	264.9	5.0

Table 5. Average and scatter of the calculated stress using equation (8) for the six indents in experiment 1.

The standard deviation is much higher for the 50 mN indents than the 200 mN indents. This is because the 50 mN indents are much smaller than the 200 mN ones and thus more susceptible to local heterogeneities such as surface roughness which cannot be removed nor quantified during sample preparation.

Twin number, indent-twin area fraction, twin number density and normalised individual twin size (cf. section 2.4.2) are tabulated in table 6 along with stress values calculated from equation (8), (maximum load divided by the indenter contact area) for all twelve 50 mN and 200 mN indents. The indent-twin area fraction is a normalised parameter that measures the amount of twin growth at the sample surface with respect to each individual indent. Similarly the twin number density is the ratio between the observed numbers of twins at the sample surface and the indent area. The normalised individual twin size measures the size of each individual twin respect to the projected indent area.

It can be observed visually in figure 19 and numerically in table 6 that 200 mN indents

yielded higher number of twins than the 50 mN indents. However when you normalise this value with respect to the indent area the 50 mN indents produced much higher twin number density. The normalised individual twin size is also higher for the higher stressed 50 mN indent. The area fraction is more difficult to compare due to variation in the 50 mN data. If we put side to side the most numerically consistent group – the 10mN/s loading rate, 50 mN indent set with indents at equivalent loading rate for 200mN, no significant difference in the twin-indent area fraction can be observed. On the other hand, when we compare between the repeats for all six indent parameters, 75% of the indents show higher twin-indent area fraction for the more highly stressed indent.

Indent			Stress, σ (MPa)	Twin number	Twin-indent area fraction (%)	Twin number density (number/m ²)	Normalised individual twin size (%)
P_{max}	\dot{P}	#					
50 mN	0.1mN/s	A	269.3	8	65.6	72.2 x10 ⁹	8.2
	0.1mN/s	B	318.6	6	49.0	85.8 x10 ⁹	8.2
	1 mN/s	A	300.7	8	78.7	67.2 x10 ⁹	9.8
	1 mN/s	B	259.4	7	56.4	70.8 x10 ⁹	8.1
	10 mN/s	A	322.0	11	72.8	107.0 x10 ⁹	6.6
	10 mN/s	B	325.0	8	88.6	64.6 x10 ⁹	11.1

(a)

Indent			Stress, σ (MPa)	Twin number	Twin-indent area fraction (%)	Twin number density (number/m ²)	Normalised individual twin size (%)
P_{max}	\dot{P}	#					
200 mN	0.1mN/s	A	239.5	17	75.7	29.6 x10 ⁹	4.5
	0.1mN/s	B	235.5	16	79.8	26.0 x10 ⁹	5.0
	1 mN/s	A	246.5	15	87.9	23.1 x10 ⁹	5.9
	1 mN/s	B	244.0	16	59.1	36.3 x10 ⁹	3.7
	10 mN/s	A	242.7	17	89.7	25.3 x10 ⁹	5.3
	10 mN/s	B	235.8	18	76.7	30.5 x10 ⁹	4.3

(b)

Table 6 - Twin number, area fraction, twin number density and normalised individual twin size calculated from optical microscopic image analysis with correlation to indent stress values for (a) 50mN, and (b) 200mN indent groups

3.3.2 Effect of varying strain rate

Results for both groups suggest that both the number and the twin-indent area fraction of twins formed were insensitive to the change in loading rate within the scatter of results and for the two orders of magnitude range in the strain rates used

here. This is consistent with the findings of Korla *et al* and Brown *et al* in magnesium and beryllium, which suggest that although strain-rate may determine if the material slips or twins, an increase in strain-rate does not affect twinning frequency and area [27, 54]. It should be noted that strain-rate is not directly compared here, rather a relative increase of it as loading rate increases at a constant maximum load.

3.4 Twin variant selection and Schmid factor

We have observed in section 3.2 that twinning is associated with the shear of material underneath the indent, and that the direction components of the shear influence the variant selection process. We observed also a correlation between twinning and the Schmid Factor calculated using the loading direction (c.f. table 4). In the next section we will further examine these two observations by reviewing the results of experiment 3 described in section 2.3.2 of indenting in the simple direction $[11\bar{2}0]$, alongside other indents made in more complex directions.

3.4.1 Indents in symmetrical direction $[11\bar{2}0]$

In experiment 3, a set of three indents was made following the simple direction $[11\bar{2}0]$ - $[0001]$ - $[\bar{1}100]$ as represented by figure 12. Two more sets of indents were

made by rotating the sample 45° and 90° , to examine the effect of shear direction (independent to tip loading direction) on the variant selection process. Optical microscopic images in figure 23 reveal similar twin propagation patterns for all three orientations: 0° , 45° and 90° . Specifically, that twin occurred on only two out of three sides of the triangular indent. These twins spread outwards evenly along $[0001]$ direction.

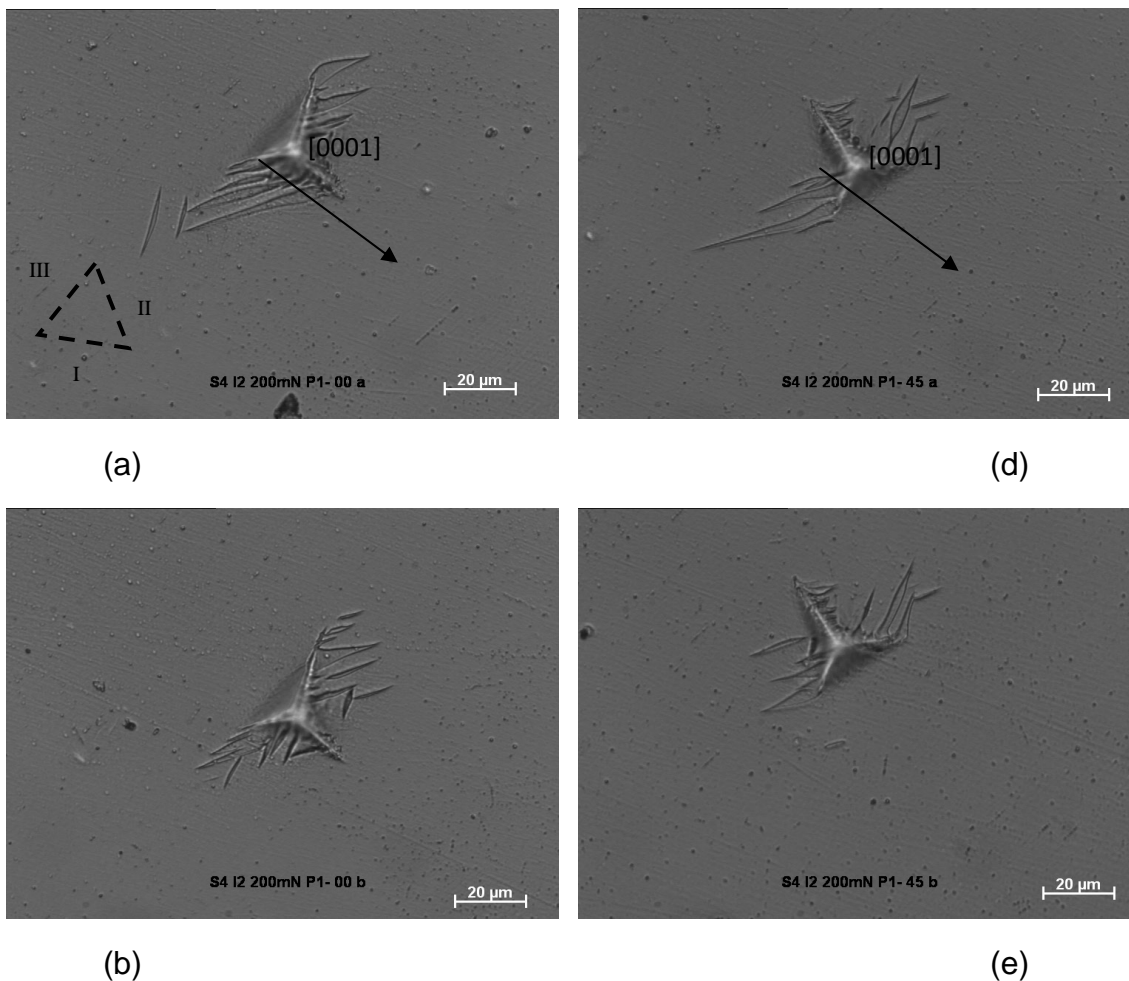
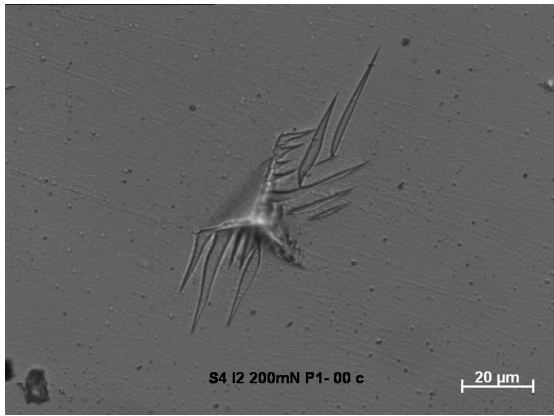
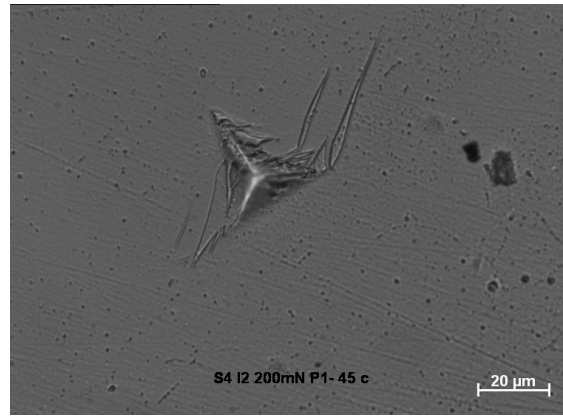


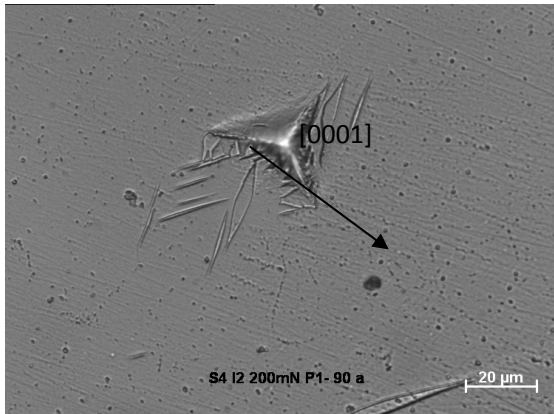
Figure 23. Optical micrographs of indents (a)~(c) 00° , (d)~(f) 45° and (g)~(i) 90° .



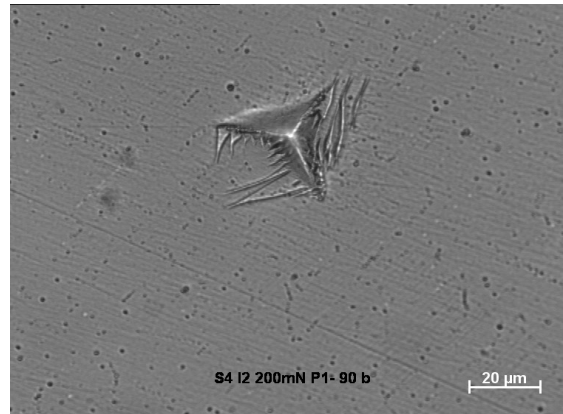
(c)



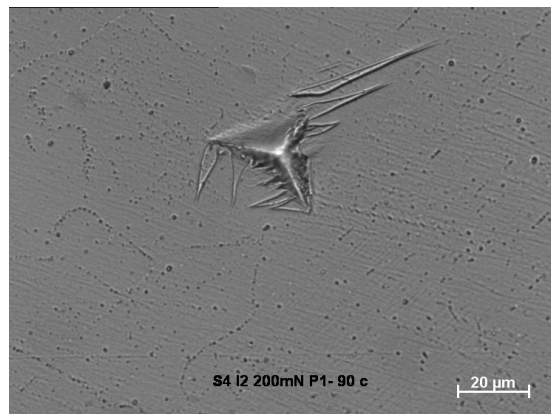
(f)



(g)



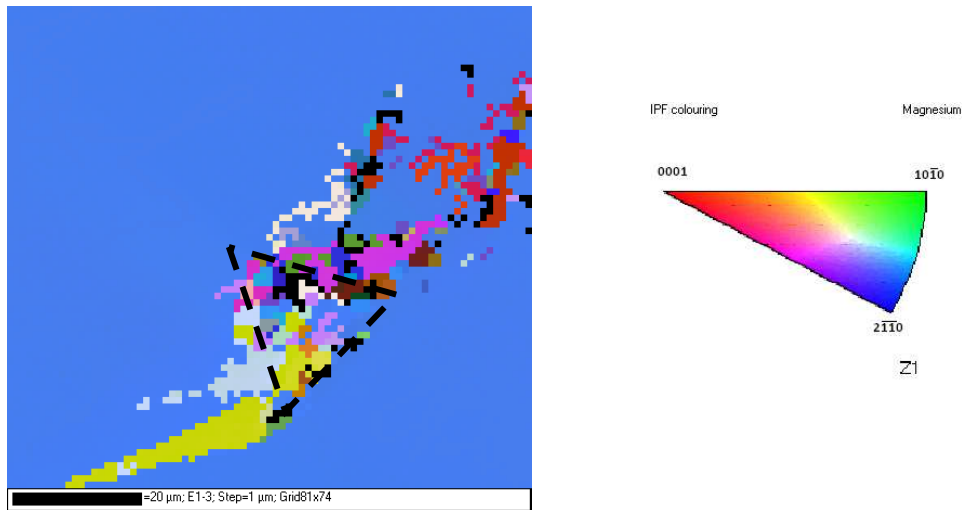
(h)



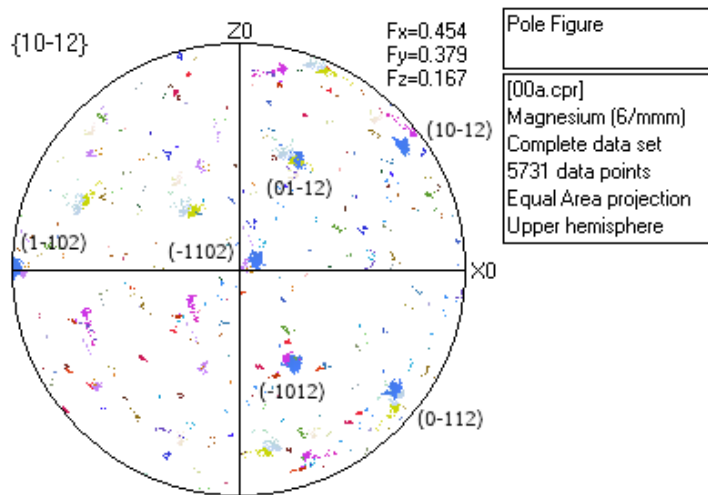
(i)

Figure 23. Optical micrographs of indents (a)~(c) 0, (d)~(f) 45 and (g)~(i) 90.

The EBSD result of a 0° indent (figure 23a) is displayed in figure 24. As stated in section 3.1 the twin variants formed are $(01\bar{1}2)$, $(0\bar{1}12)$, $(10\bar{1}2)$ and $(\bar{1}012)$. EBSD revealed that similar twin variants had formed in the 45° and 90° orientation indents.



(a)



(b)

Figure 24. (a) Optical micrograph and EBSD scan of the 00a indent. Variants corresponding to the indents are labelled on the optical micrograph. (b) The pole figure used to identify the variants.

3.4.2 Variant selection for other indents

If twin nucleation is dependent on the loading direction (sample normal direction), the Schmid factor (SF) calculation may be useful to indicate the twin variants formed in the other indentation experiments. Here the results obtained for three loading directions: $[7 \bar{5} \bar{2} \bar{2}]$, $[1 2 \bar{3} 1]$ and $[\bar{1} 3 \bar{2} \bar{2}]$, using optical microscopy, EBSD are presented together with SF calculations. Figures 25 to 27 display the EBSD results and table 7 lists the SFs and twinning frequency in each indentation test. Frequency here refers to the percentage of twin variants observed as the number of indents made varied with direction.

Contrary to the observation in the previous section, table 7 suggests that twin nucleation is unrelated to the Schmid criterion.

Tension twin variants	$[7 \bar{5} \bar{2} \bar{2}]$		$[1 2 \bar{3} 1]$		$[\bar{1} 3 \bar{2} \bar{2}]$	
	m	frequency	m	frequency	m	Frequency
(10-12)	0.415	50%	0.213	40%	-0.161	0
(01-12)	-0.003	25%	0.359	40%	0.101	100%
(-1012)	0.393	0%	0.182	80%	-0.149	0
(0-112)	-0.007	25%	0.321	100%	0.158	0
(1-102)	0.279	0%	-0.044	40%	0.046	50%
(-1102)	0.261	25%	-0.036	100%	0.000	50%

Table 7. Schmid Factor (m) and twinning frequency for three sample normal directions $[7 \bar{5} \bar{2} \bar{2}]$, $[1 2 \bar{3} 1]$, and $[\bar{1} 3 \bar{2} \bar{2}]$.

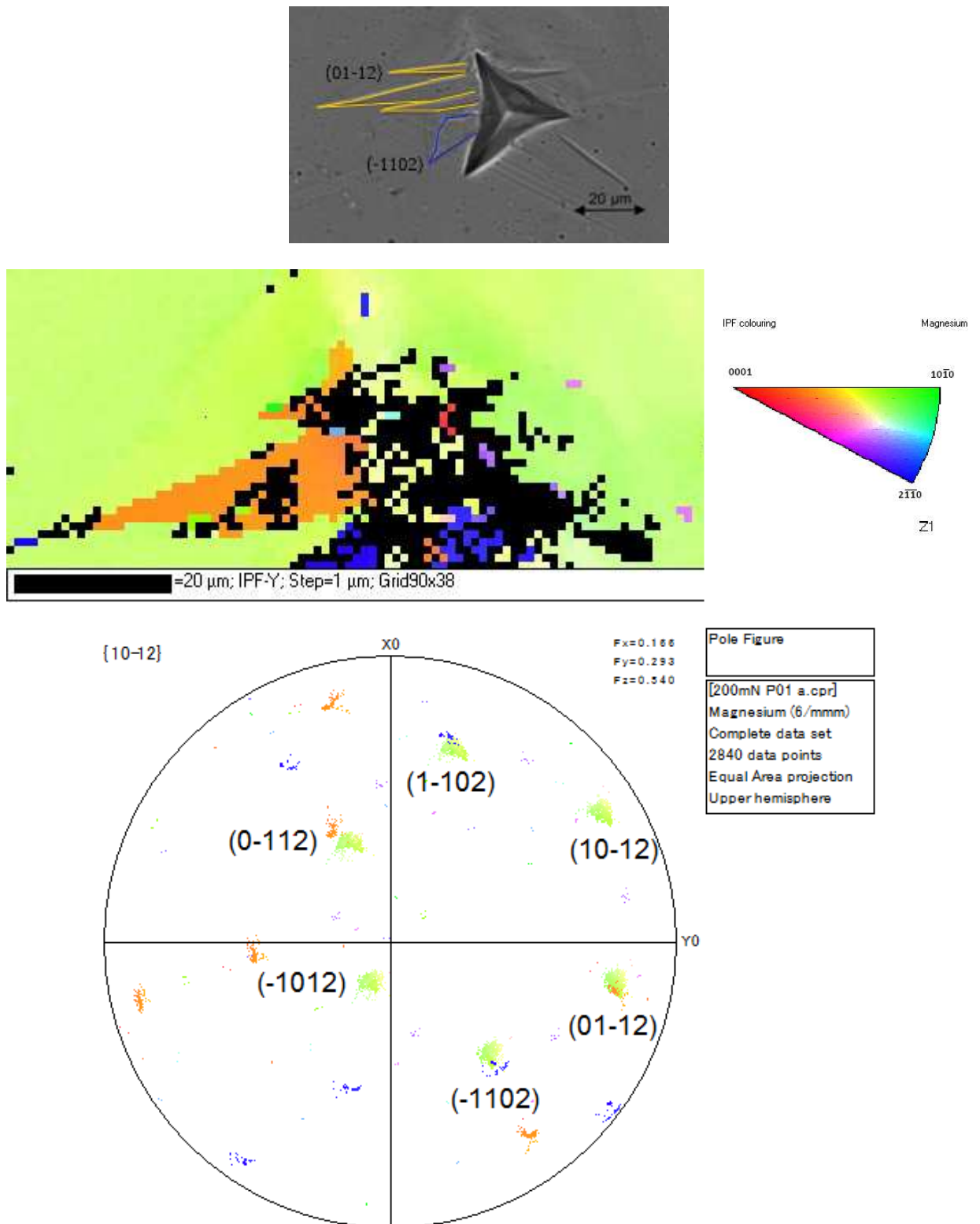


Figure 25. Optical micrograph and EBSD results obtained from the sample indented up to 200 mN with the loading rate of 0.1 mN/s. The loading direction is along $[7 \bar{5} \bar{2}]$.

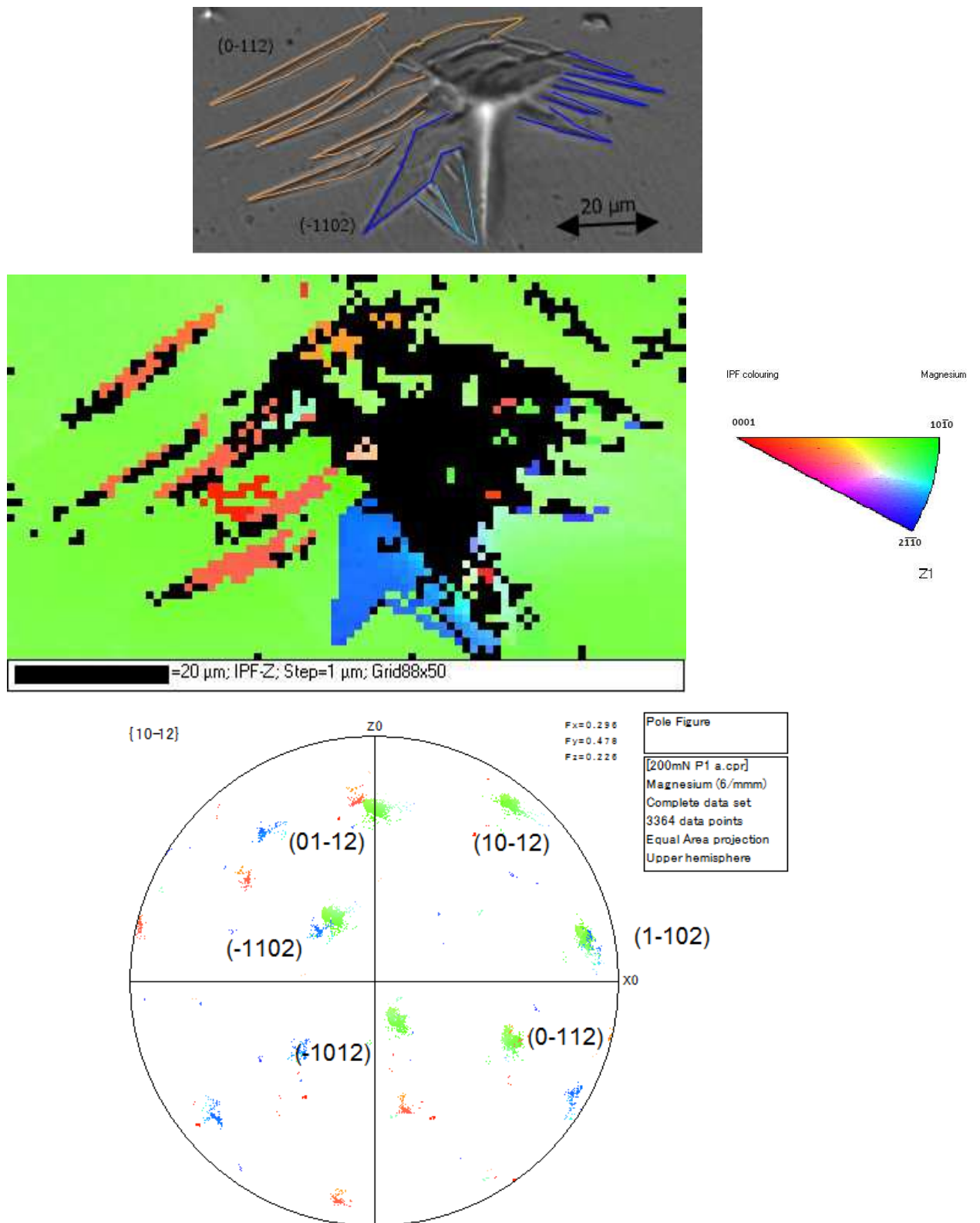


Figure 26. Optical micrograph and EBSD results obtained from the sample indented up to 200 mN with the loading rate of 1 mN/s. The loading direction is along $[1\ 2\ \bar{3}\ 1]$.

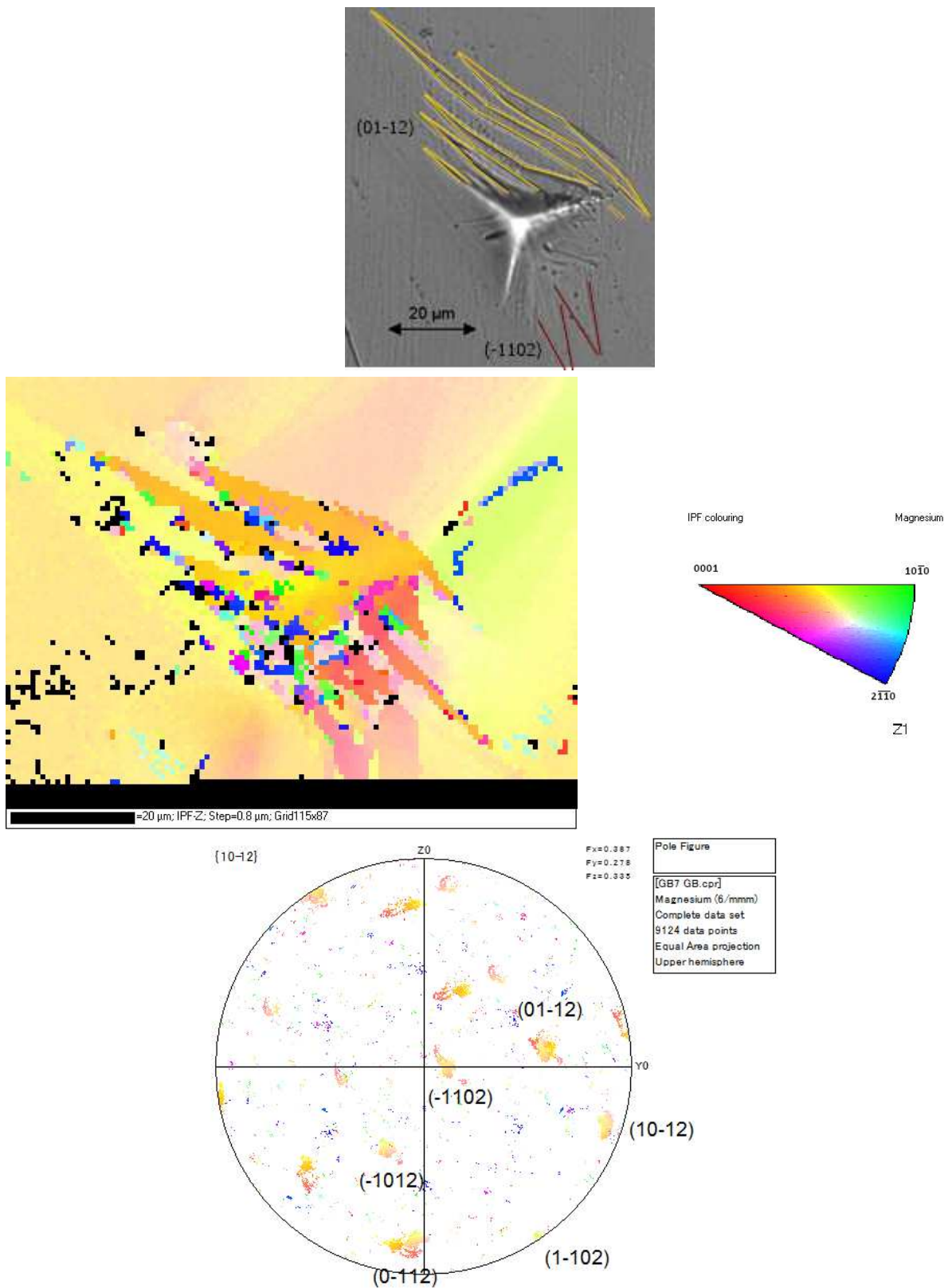


Figure 27. Optical micrograph and EBSD results obtained from the sample indented up to 200 mN with the loading rate of 1 mN/s. The loading direction is along $[\bar{1} \ 3 \ \bar{2} \ \bar{2}]$

3.5 Effect of grain and twin boundaries

Figure 28 shows the grains and twin boundaries indented as described in section 2.3.3. The boundaries are highlighted in red. Optical micrographs of indents made on the 14° and 80° grain boundaries in figure 29 show no effect on twin nucleation and growth at the nearby boundaries (pre-existing indents were carefully examined and labelled where necessary). Note that the grain boundary indents were done twice due to calibration problems in the first run. Figure 30 shows the indents for GB- 32° . Figure 30 (c) shows the presence of several grain-boundary related twins that appeared after the indentation test, when an indent (GB- 32° T3) was made near the 32° grain boundary.

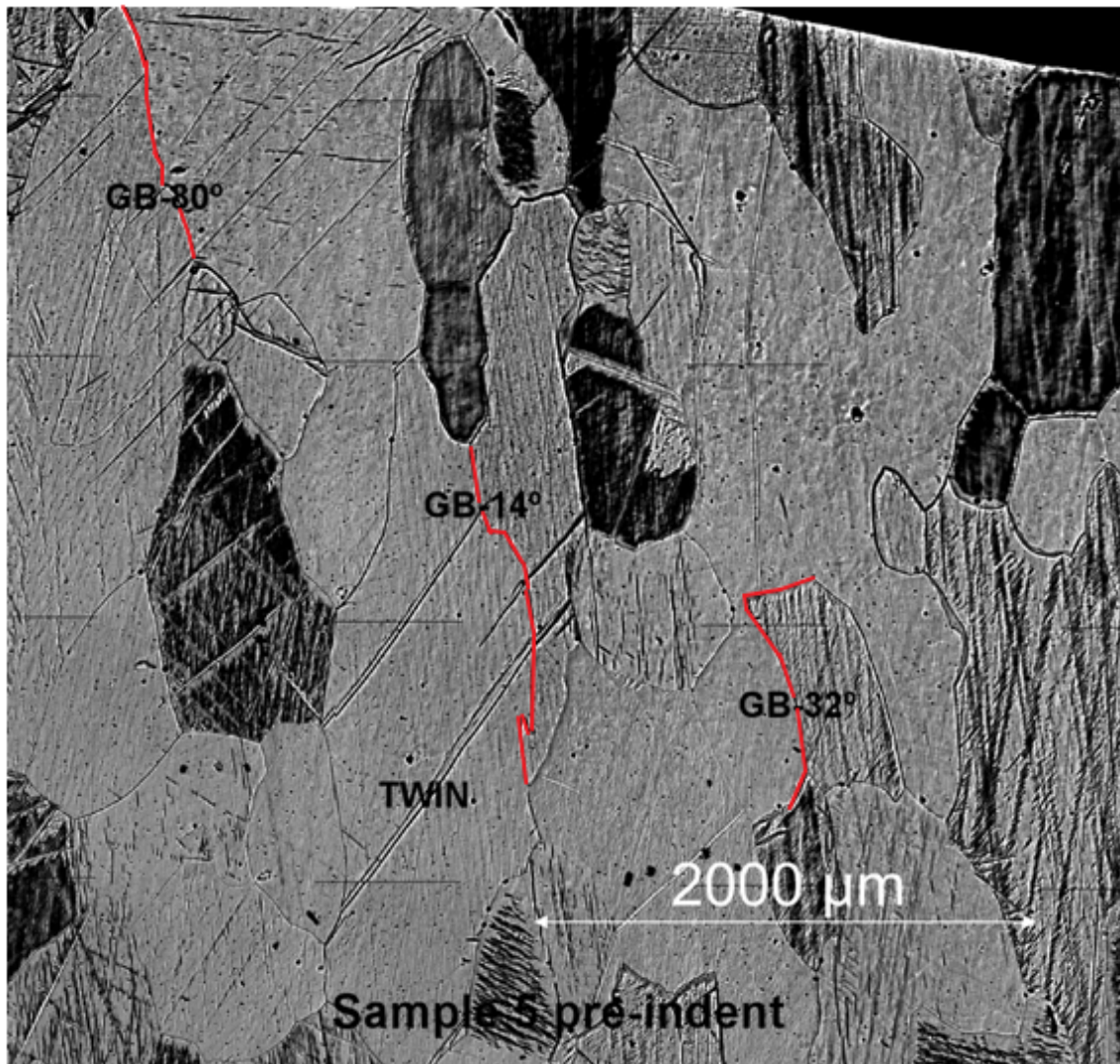
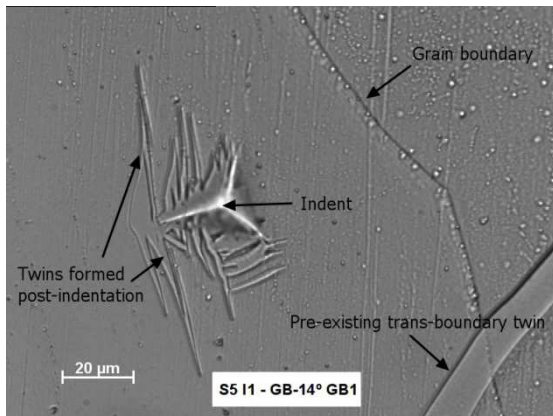
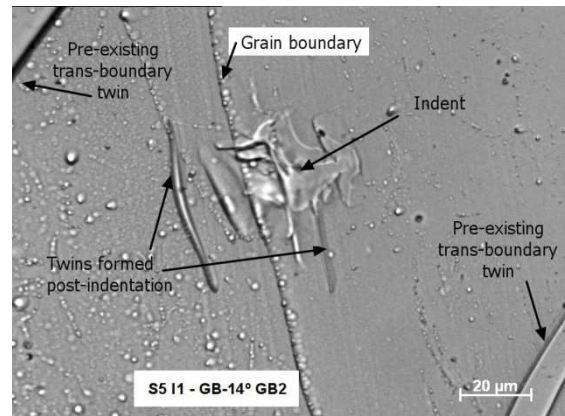


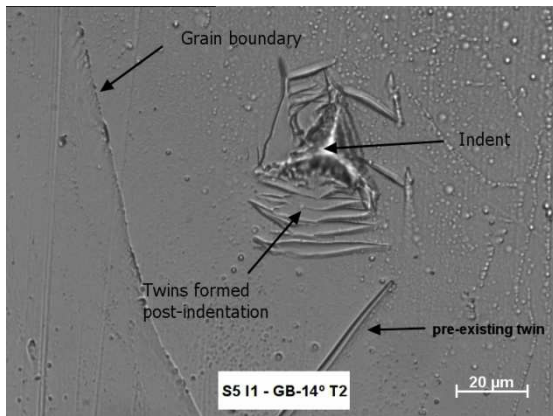
Figure 28. Optical micrograph of grain and twin boundaries selected for indentation (red).



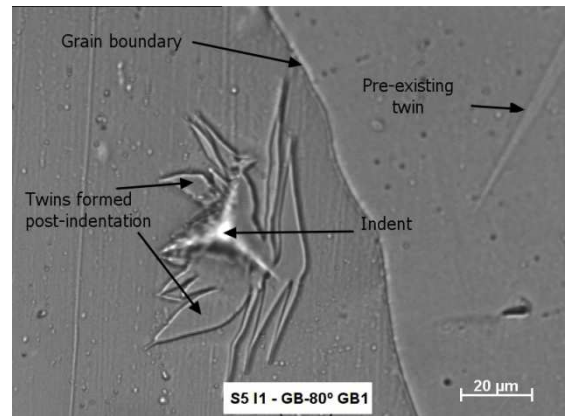
(a)



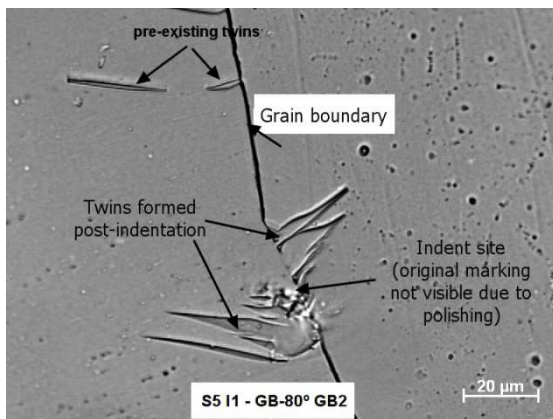
(b)



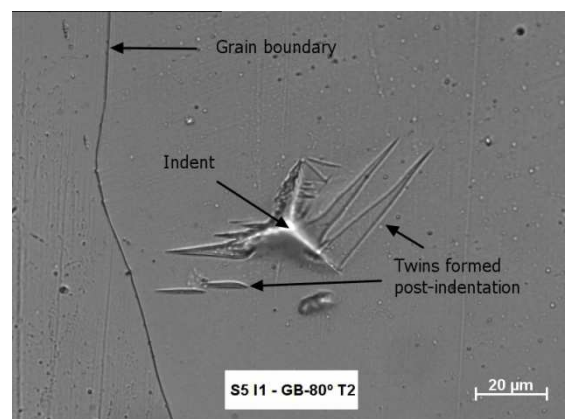
(c)



(d)

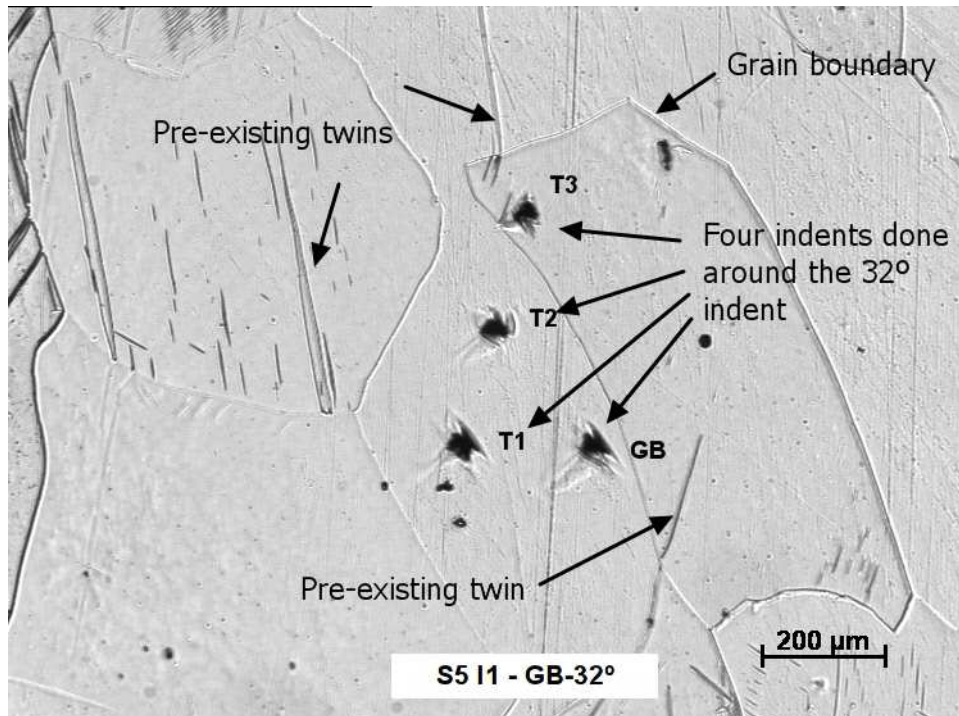


(e)

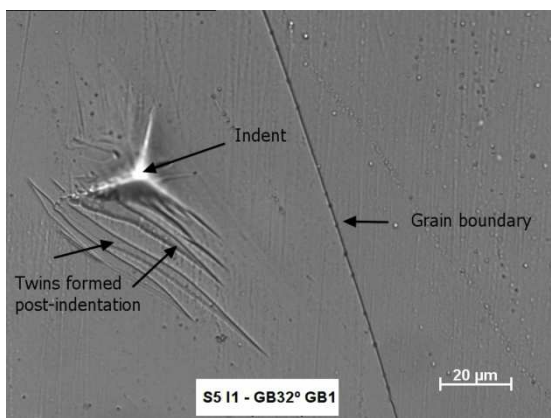


(f)

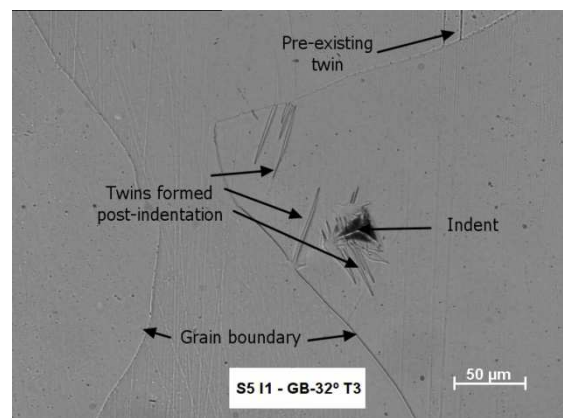
Figure 29. Indents made across GB-14° and GB-80°. Only indents made in close proximity to the grain boundaries are shown, (a) first attempt at GB-14° indent, (b) second attempt at GB-14° indent, (c) near boundary indent for GB-14°, (d) first attempt of GB-80° indent, (e) second attempt of GB-80° indent and (f) trans-boundary indent for GB-80°



(a)



(b)



(c)

Figure 30. Optical micrographs of GB-32° indents. (a) shows location of indents with respect to GB-32° (b) first attempt of GB-32° indent, (c) indent GB-32° T3.

EBSD analysis in figure 31 revealed that $(01\bar{1}2)$ and $(\bar{1}102)$ were the two main twin variants formed by the GB-32° T3 indent. The $(\bar{1}102)$ twin was related to both the indent and the grain boundary surrounding the indent. Adjoining twins in the

neighbouring grains (marked by red arrows) were also observed. The joined twins are not of the same variant according to EBSD: shown the top red arrow in figure 31, are joined by the top variant ($\bar{1}102$) and the bottom variant ($0\bar{1}12$).

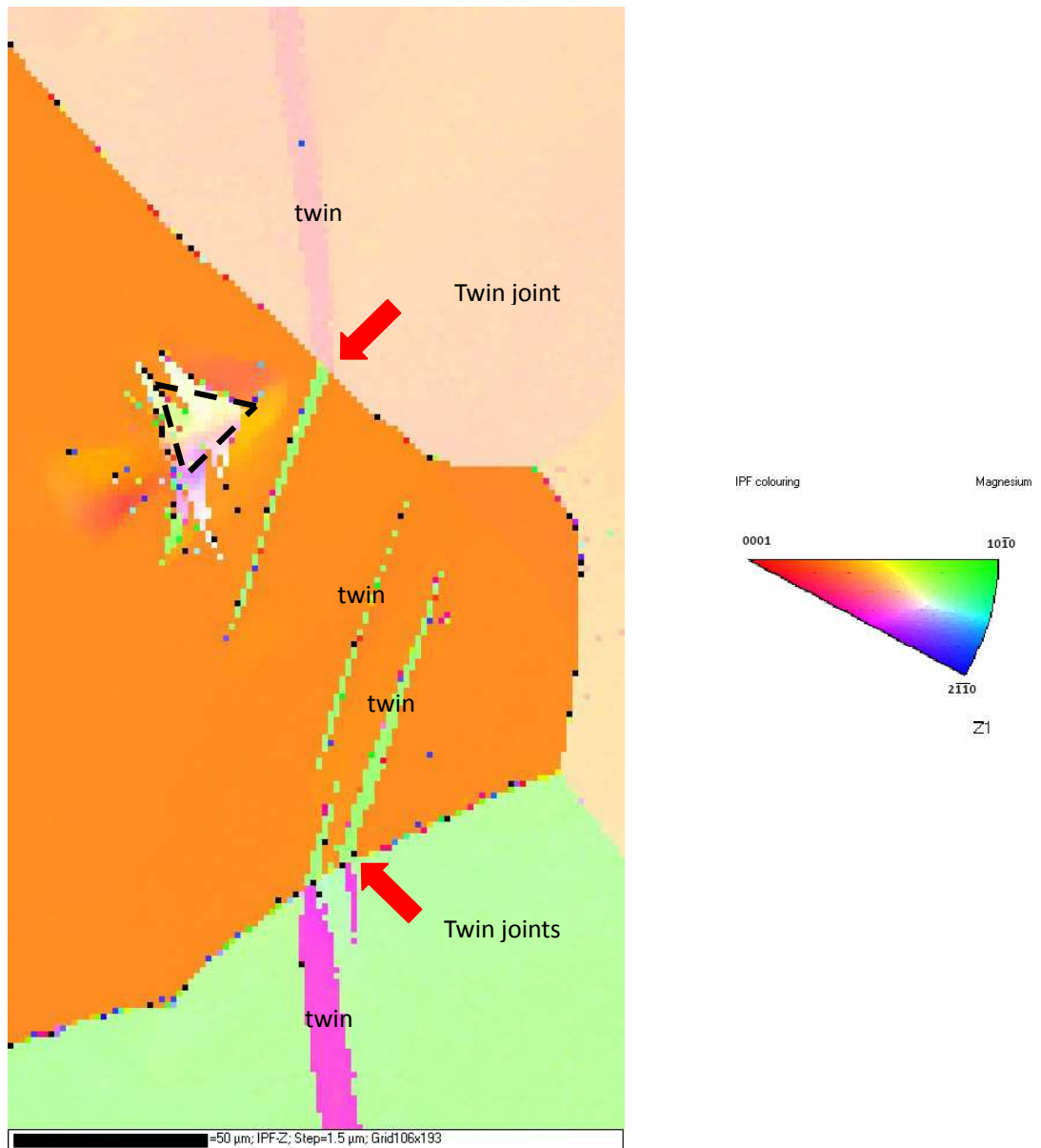


Figure 31. EBSD results for the GB-32° T3 indent. The colour orange represent the matrix, pink and green are the neighbouring grains, at the top red arrow, the twin in green is the ($\bar{1}102$) twin and in pink is the ($0\bar{1}12$) twin.

Indenting on a twin boundary (figure 32) did not nucleate further twins near the surrounding boundaries. In fact, the indent made produced a much smaller number of twins around the immediate indent area in comparison to other indents made on the same grain. The indent did however permanently alter the shape of the pre-existing twin. This is due to the material flow mechanism under the indent as described in section 3.1.



Figure 32. Indent at a twin boundary.

CHAPTER 4. DISCUSSION

4.1 Occurrence of twins

Tension twins $\{10\bar{1}2\}$ had formed around all indents in the current study, as suggested in the literature. This is attributed to the relatively lower energy required for shear and shuffle in comparison to compression twinning $\{10\bar{1}1\}$ and all other twinning modes (c.f. table 2). The observation could also reflect on the relative CRSS difference found between the two modes in other studies where compression twins require some three times higher stress to activate [11, 38]. The compression twins $\{10\bar{1}1\}$ in figure 33, found in very small quantity at the edges of tension twins in an indent made along the $[\bar{1}3\bar{2}\bar{2}]$ direction, were absent around other indents on the same grain. It is possible that $\{10\bar{1}2\}$ - $\{10\bar{1}1\}$ double twins had formed - but since this was observed but only once indicates it is unlikely to be the dominant mechanism. The double twins found in this study could be the result of tension twins interacting with one another due to geometry hence do not contribute to any increase in the strain accommodating abilities of magnesium.

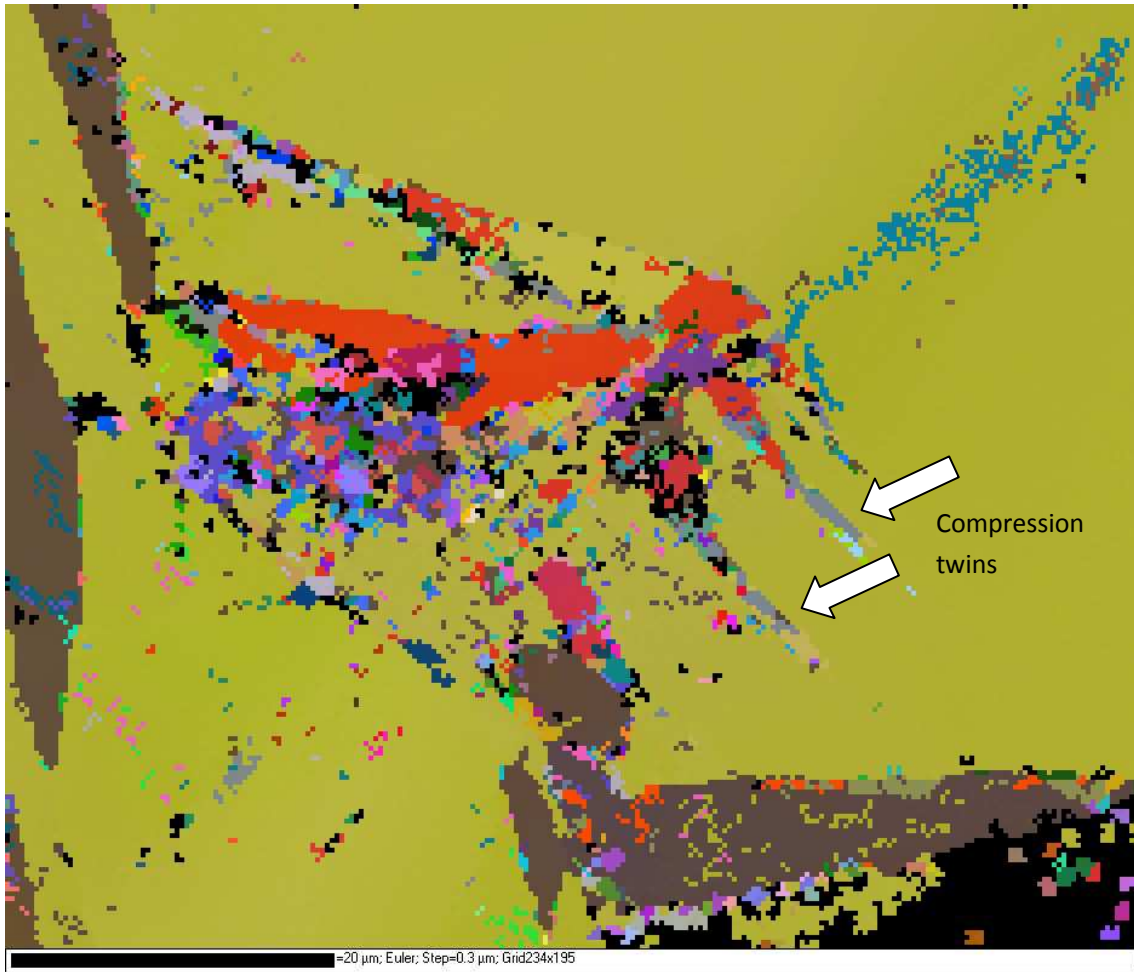


Figure 33. EBSD scan in euler colours showing an indent containing both tension twins $\{10\bar{1}2\}$ in red and brown, and compression twin $\{10\bar{1}1\}$ in grey.

In section 3.4.2 we have reported the occurrence of four twin variants which is consistent with the SF calculation. Similar results have also been reported by Kang *et al* for nanoindentating steel using a spherical indenter. However, it should be noted that in this study, using figure 20 as an example, the four twin variants occurred in different popularity, as well as their position relative to the indent. The twin variants $(\bar{1}012)$ in pink and $(0\bar{1}12)$ in light blue are more popular, and in closer proximity to the indent than twin variants $(10\bar{1}2)$ in red, and $(01\bar{1}2)$ in yellow. This behaviour is

consistent to the repeated indents in the same orientation. There is an evident inconsistency between our result and the absolute Schmid behaviour - that all four twin variants have equal likelihood to form (c.f. table 4). One may argue the validity of the SF consideration in the case of nanoindentation using a Berkovich indenter. So far, the SF consideration has given a good first order estimation of the twin variant selection based on the loading direction with regards to the sample surface. Yet the simplified approximation does not take into account the indenter geometry and material properties that render the stress and strain distribution underneath the indent, which is likely differ from the expected twinning behaviours - e.g. the twin growth and therefore the observed popularity and position difference of the four variants observed.

4.2 Effect of varying stress and strain rate on twinning

4.2.1 Effect of varying stress

It has been shown in this study that stress concentration such as a nano-indent introduces of twinning in magnesium. Many studies of deformation twins previously have discussed stress concentration to have positive effect on twin frequency and twinning area fraction [14, 39, 42],. Yet our own observations on the effect of mean stress (induced by the indentation size effect (reference on ISE)) show some

discrepancy (c.f. section 3.3.1).

In the current study, the number of twins decreases with the mean stress value. This value, in fact, has no direct relationship with the mean stress but instead should be comprehended as the result of increase in volume of materials involved during plastic deformation at larger indentation size.

On the other hand, the twin number density increases with the mean stress - suggesting a direct correlation between higher mean stress (329.3 MPa) and increase in twin nucleation. The normalised individual twin size has also increased with mean stress. This parameter characterises the growth of an individual twin with respect to varying load. More, and larger twins have formed on average per area unit for the higher stress experiments.

As previously mentioned, when the indentation size is small, the mean stress applied is much larger than that under a large indent size (ISE of mean stress/hardness). We observe that twin nucleation and growth in the current study are both more effective under the larger mean stress. This resembles Capolungo's energy considerations in figure 5, that an initial energy barrier is required before a stable twin nucleus is formed; and that the maximum attainable twin volume is determined by an external stress state. Higher mean stress corresponds to higher instantaneous energy exerted on the

material and thus the energy barrier, E_{activ} is satisfied for more twin nuclei to form. The high mean stress also determines the external energy state and therefore dictates in our case twin size, in 2-dimensions

The twin indent-area fraction accounts for the normalised total fraction of twin that had formed as a result of indentation. Here the twin indent-area fraction is independent from change in mean stresses. In this case the higher mean stress attributed to indentation size effect is not comparable to a higher stress imposed on the material in uniaxial tension or compression tests as maximum strain under any indent is constant, at 8% [57], whereas in uniaxial tension or compression tests strain increases proportional to stress. However, in between the repeated indents, 75% of the more highly stressed indents showed higher indent-twin area fraction. This does suggest a positive effect of maximum stress on twinning but the uncertainty associated with the remaining part of the data-set allows us to draw no conclusion.

We must also consider a more fundamental limitation to our existing data-set - that only superficial twins are considered here. Yet in fact the indents made are three-dimensional and complex in geometry from a Berkovich tip. Time constraints restricted 3-D mapping of the volume around the indent but this can certainly give more accurate accounts for the twin development around the indent. Furthermore the complexity associated with loading directions of each facet on the magnesium may

be ameliorated by using a simple spherical or conical tip for indentation.

4.3 Twin variant selection and Schmid factor

4.3.1 Variant selection with respect to indents in $[11\bar{2}0]$, $[7\bar{5}\bar{2}\bar{2}]$, $[12\bar{3}1]$, and $[\bar{1}3\bar{2}\bar{2}]$ directions.

Twin variant selection of indents on grains with sample directions $[11\bar{2}0]$, follows closely to the SF consideration. However, when different loading directions were examined, i.e. $[7\bar{5}\bar{2}\bar{2}]$, $[12\bar{3}1]$, and $[\bar{1}3\bar{2}\bar{2}]$, twins associated with low Schmid factor - therefore not predicted to occur, were found in abundance. It is interesting to note that the breaking down of the Schmid criterion in twinning was also observed by Jonas *et al* in the uniaxial tensile deformation of magnesium alloys AZ30 and AM30 deformed in tension [11]. They explain their findings using a numerical simulation that calculated the accommodation strains at the grain boundaries twinning imposes due to the length change associated with equation 2 in section 1.1.1. However in our study we have carefully placed the indents away from the grain boundary to create a quasi-single crystal condition at which the dislocations generated during indentation should have no interaction with any grain boundaries and therefore the accommodation strain theory is not applicable here.

An attempt has been made to understand the twinning behaviour using Johnson's cavity model [58], where the material is assumed to be isotropic and only the stresses at the surface of the materials were considered [59]. This method produced consistent results with the Schmid Factor calculation. However, similar to the SF model mentioned earlier the cavity model is also over simplified in that magnesium has a highly anisotropic hexagonal structure.

As a future work, it is worthwhile to build a physically sound numerical model to predict the twinning induced by nanoindentation in magnesium. This can be further incorporated with the 3D characterisation of the twins under the indent using the FIB/EBSD technique.

4.4 Grain boundary and twin boundary

4.4.1 Effect of grain boundary

We found that a stress concentration (indent) on or near a grain boundary would induce twinning immediately around the indent in the same way as when indenting in the middle of the grain. We also found that indenting on or near a low angle grain boundary ($< 30^\circ$), with existing twins in the neighbouring grains would trigger twin nucleation and growth at a grain boundary some distance away from the indent. The

newly formed indent would associate closely to the indent in the neighbouring grain forming an adjoining-twin-pair (ATP). This is consistent with Beyerlein's observation of adjoining twin pairs (ATP) and the grain-boundary misorientation threshold of 30° [14]. Grain boundaries with existing twins are more susceptible to further twinning as the existing twin introduces a local stress concentration where it meets the grain boundary.

EBSB results revealed that the ATPs are of different variants which indicate that the two twins are indirectly related to one another, and are nucleated from separate twin embryo. This again proves that the original, pre-existing twin may act as a local stress concentration at the grain boundary and when the neighbouring grain is stressed a new twin may nucleate due to this stress concentration. This domino-effect like behaviour further elucidates the catastrophic nature of twinning macroscopically.

The grain boundary effect can be further, more systematically explored given more time, incorporating our current conclusions on the effects of ATPs. This would provide invaluable insights into the relationship between grain boundary angles and twin propagation, possibly opening a new process route to control twinning.

4.4.2 Effect of twin boundary

Based on our observations, a twin boundary would be a less likely place for twins to nucleate and grow in comparison to a grain boundary. Not only were there no twins formed beyond the immediate area surrounding the indent, but the indent triggered fewer twins around the indented area than expected. Twins formed due to the indent did not penetrate into the pre-existing twin to form double twins.

Alteration to the pre-existing twin shown in figure 32 presents an opportunity further investigate twin-boundary response to external stress using perhaps micro-scale instead of nano-scale indentation as previous studies on grain boundary indents have not reported the above observation.

CHAPTER 5. CONCLUSIONS

Here we conclude the study of deformation twinning in pure magnesium using nano-indentation. Our primary goals were to observe the effects on twinning of local stress concentration, strain rate, crystal orientation, grain boundary and pre-existing twins using controlled indentation. A Berkovich tip was employed and the indents were characterised using optical microscope, SEM and EBSD.

We have successfully induced twinning with all indents made on the magnesium samples. The dominant twinning mode was tension twin $\{10\bar{1}2\}$ with one observation of compression twin $\{10\bar{1}1\}$ and some double twinning $\{10\bar{1}2\} - \{10\bar{1}2\}$ via intersection. This was true regardless of crystal orientation, and the magnitude of the applied stress and strain. The induced twinning patterns were highly reproducible.

Using an indent in the simple direction $[11\bar{2}0]$ as example, we described a scenario to rationalise twin nucleation and growth process with respect to magnesium's response to the intruding indent tip. Material flow direction changes as the indent tip sinks into the magnesium, promoting the growth of different twin variants as twinning is highly directional. Twin variants $(1\bar{1}02)$ and $(\bar{1}102)$ was not observed for any $[11\bar{2}0]$ direction indents as the shear planes for these two systems were parallel to the loading direction.

Despite twinning occurring with every indent, we have found no solid conclusion that increasing the maximum contact stress, using the size-effect phenomenon with nano-indentation, has an effect on twinning. Two indent groups, one with an average contact stress of 329.3 MPa and the other lower at 264.9 MPa showed conflicting results within group, and between groups. We believe that the indentation might not be the most appropriate method to observe the effect of higher stress concentration as it is not possible to increase strain beyond 8%.

One limitation to be overcome is that we have only accounted the superficial twins at the sample surface. A three-dimensional study of the indent using a combination of focused ion beam and EBSD would enable the entire plastic zone volume to be analysed but this was out of the time-scope of the current study.

We have found that twinning is strain-rate insensitive which conforms to other twinning studies summarised in section 1.3.2.1 of this thesis.

This study has again observed the breakdown of the Schmid criterion for deformation twinning in magnesium. The Schmid criterion here predicted only twin nucleation of indents made in the simple direction $[11\bar{2}0]$. We suspect that complex stress field underneath the indent requires more vigorous and in-depth computing to resolve. How twins form with respect to the stress field under the indent cannot be analysed

until first a good understanding of the stress field under the indent. Another way to simplify this is to use an indenter tip of simpler geometry, such as a spherical or conical tip for further studies.

We have observed that grain boundaries with existing twins are more susceptible to further twinning as the existing twin introduces a local stress concentration where it meets the boundary. As one grain boundary touching twin triggers twinning in the neighbouring grain, a domino-like effect is observed, explaining the catastrophic nature of the macroscopic twinning process.

Lastly, twin boundaries have no apparent effect on promoting twinning. We however observed a permanent alternation of the pre-existing twin indented which can be further explored to understand the twin-boundary response to external stress.

Reference

1. Fischer, F.D., Schaden, T., Appel, F., Clemens, H. (2003), "Mechanical twins, their development and growth", *European Journal of Mechanics A/Solids* **22**, 709-726
2. Christian, J.W., Mahajan, S. (1995), "Deformation twinning", *Progress in Materials Science* **39**, 1-157
3. Chun, Y.B., Yu, S.H., Semiatin, S.L., Hwang, S.K. (2005), "Effect of deformation twinning on microstructure and texture evolution during cold rolling of CP-titanium", *Materials Science and Engineering A* **398**, 209-219
4. Mendelson, S. (1970), "Dislocation Dissociation in hcp Metals", *Journal of applied physics* **41**, 1893-1910
5. Yoo, M.H., Morris, J.R., Ho, K.M., Agnew, S.R. (2002), "Nonbasal Deformation Modes of HCP Metals and Alloys: Role of Dislocation Source and Mobility", *Metallurgical and Materials Transaction A* **33A**, 813-822
6. Wan, G., Wu, B.L., Zhao, Y.H., Zhang, Y.D., Esling, C. (2011), "Strain-rate sensitivity of textured Mg-3.0Al-1.0Zn alloy (AZ31) under impact deformation", *Scripta Materialia* **63**, 461-464
7. Beyerlein, I.J., Wang, J., Barnett, M.R., Tomé, C.N. (2012), "Double twinning mechanisms in magnesium alloys via dissociation of lattice dislocations", *Proceedings of the Royal Society A* **468**, 1496-1520
8. Meyers, M.A., Vöhringer, O., Lubarda, V.A. (2001), "The onset of twinning in

- metals: a constitutive description”, *Acta Materialia* **49**, 4025-4039
9. Wang, J., Beyerlein, I.J., Tomé, C.N. (2010), “An atomic and probabilistic perspective on twin nucleation in Mg”, *Scripta Materialia* **63**, 741-746
 10. Cahn, R.W. (1954), “Twinned Crystals”, *Advances in Physics* **3:12**, 363-445
 11. Jonas, J.J., Mu, S., Al-Samman, T., Gottstein, G., Jiang, L., Martin, É (2011), “The role of strain accommodation during the variant selection of primary twins in magnesium”, *Acta Materialia* **59**, 2046-2056
 12. Bell, R.L., Cahn, R.W. (1957) “The dynamics of twinning and the interrelation of slip and twinning in zinc crystals”, *Proceedings of the Royal Society of London. Series A, Mathematical and Physical Sciences* **239**, 494-521
 13. Nave, M.D., Barnett, M.R. (2004), “Microstructures and textures of pure magnesium deformed in plain-strain compression”, *Scripta Materialia* **51**, 881-885
 14. Beyerlein, I.J., McCabe, R.J., Tomé, C.N. (2011), “Effect of microstructure on the nucleation of deformation twins in polycrystalline high-purity magnesium: A multi-scale modelling study”, *Journal of the Mechanics and Physics of solids* **59**, 988-1003
 15. Barnett, M.R., Keshavarz, Z., Beer, A.G., Ma, X. (2008), “Non-Schmid behaviour during secondary twinning in a polycrystalline magnesium alloy”, *Acta Materialia* **56**, 5-15
 16. Bilby, B.A., Crocker, A.G. (1965), “The theory of the crystallography of deformation twinning”, *Proceedings of the Royal Society of London. Series A, Mathematical*

and Physical Sciences **288**, 240-255

17. Serra, A., Bacon, D.J., Pond, R.C. (1988), "The crystallography and core structure of twinning dislocations in H.C.P. metals", *Acta Materialia* **36**, 3183-3203
18. Clark, R., Craig, G.B. (1952), "Twinning", *Progress in metal physics* **3**, 115-139
19. Ulacia, I., Dudamell, N.V., Gálvez, F., Yi, S., Pérez-Prado, M.T., Hurtado, I. (2010), "Mechanical behaviour and microstructural evolution of a Mg AZ31 sheet at dynamic strain rates", *Acta Materialia* **58**, 2988-2998
20. Yu, Q., Qi, L., Chen, K., Mishra, R.K., Li, J., Minor, A.M. (2012), "The nanostructured origin of deformation twinning", *Nano letters* **12**, 887-892
21. Karaman, I., Yapici, G.G., Chumlyakov, Y.I., Kireeva, I.V. (2005), "Deformation twinning in difficult-to-work alloys during severe plastic deformation", *Materials Science and Engineering A* **410-411**, 243-247
22. Gough, H.J., Cox, H.L. (1929), "The behaviour of a single crystal of zinc subjected to alternating torsional stresses", *Proceedings of the Royal Society of London. Series A, Mathematical and Physical Sciences* **123**, 143-167
23. Koike, J. (2005), "Enhanced deformation mechanisms by anisotropic plasticity in polycrystalline Mg alloys at room temperature", *Metallurgical and Materials Transactions A* **36A**, 1689-1696
24. Yoo, M.H. (1981), "Slip, twinning, and fracture in hexagonal close-packed metals", *Metallurgical Transactions A* **12A**, 409-418
25. Jiang, L., Jonas, J.J., Mishra, R.K., Luo, A.A., Sachedv, A.K., Gode, S. (2007),

- “Twinning and texture development in Mg alloys subjected to loading along the three different strain paths”, *Acta Materialia* **55**, 3899-3910
26. Hong, S., Park, S.H., Lee, C.S. (2010), “Role of {10-12} twinning characteristics in the deformation behaviour of a polycrystalline magnesium alloy”, *Acta Materialia* **58**, 5873-5885
27. Brown, D.W., Beyerlein, I.J., Sisneros, T.A., Calusen, B., Tomé, C.N. (2012), “Role of twinning and slip during compressive deformation of beryllium as a function of strain rate”, *International journal of Plasticity* **29**, 120-135
28. Ma, Q., El Kadiri, H., Oppedal, A.L., Biard, J.C., Horstemeyer, M.F., Cherkaoui, M. (2011), “Twinning and double twinning upon compression of prismatic textures in a AM30 magnesium alloy”, *Scripta Materialia* **64**, 813-816
29. Reed-Hill, R.E. (1964), *Physical metallurgy principles*. D. Van Nostrand Company, INC.
30. Bolling, G.F., Richman, R.H. (1965), “Continual mechanical twinning-Part I: Formal description”, *Acta Metallurgica* **13**, 709-722
31. Biggs, W.D., Pratt, P.L. (1958), “The deformation and fracture of alpha-iron at low temperatures”, *Acta Metallurgica* **6**, 694-703
32. Heo, T.W., Wang, Y., Bhattacharya, S., Sun, X., Hu, S., Chen, L. (2011), “A phase-field model for deformation twinning”, *Philosophical Magazine Letters* **91**, 110-121
33. Müllner, P., Solenthaler, C. (1997), “On the effect of deformation twinning on

- defect densities”, *Materials Science and Engineering A* **230**, 107-115
34. Capolungo, L., Beyerlein, I.J. (2008), “Nucleation and stability of twins in hcp metals”, *Physical review B* **78**, 024117
35. Wang, L., Eisenlohr, P., Yang, Y., Bieler, T.R., Crimp, M.A. (2010), “Nucleation of paired twins at grain boundaries in titanium”, *Scripta Materialia* **63**, 827-830
36. Korka, R., Chokshi, A.H. (2010), “Strain-rate sensitivity and microstructural evolution in a Mg-Al-Zn alloy”, *Scripta Materialia* **63**, 913-916
37. Dudamell, N.V., Ulacia, I., Gálvez, F., Yi, S., Bohlen, J., Letzig, D., Hurtado, I., Pérez-Prado, M.T. (2011), “Twinning and grain subdivision during dynamic deformation of a Mg AZ31 sheet alloy at room temperature”, *Acta Materialia* **59**, 6949-6962
38. Chapuis, A., Driver, J.H. (2011), “Temperature dependency of slip and twinning in plane strain compressed magnesium single crystals”, *Acta Materialia* **59**, 1986-1994
39. Bilby, B.A., Entwisle, A.R. (1954), “The formation of mechanical twins”, *Acta metallurgica* **2**, 15-19
40. Beyerlein, I.J., Capolungo, L., Marshall, P.E., McCabe, R.J., Tomé, C.N. (2010), “Statistical analyses of deformation twinning in magnesium”, *Philosophical Magazine* **90**, 2161-2190
41. Honeycombe, R.W. (1968), *The plastic deformation of metals*. London: Edward Arnold.

42. Zhang, R.Y., Daymond, M.R., Holt, R.A. (2011), "Parametric study of stress state development during twinning using 3D finite element modelling", *Materials Science and Engineering A* **528**, 2752-2735
43. Ghaderi, A., Barnett, M.R. (2011), "Sensitivity of deformation twinning to grain size in titanium and magnesium", *Acta Materialia* **59**, 7824-7839
44. Dobroň, P., Chmelik, F., Yi, S., Parfenenko, K., Letzig, D., Bohlen, J. (2011), "Grain size effects on deformation twinning in an extruded magnesium alloy tested in compression", *Scripta Materialia* **65**, 424-427
45. Barnett, M.R., Nave, M.D., Ghaderi, A. (2012), "Yield point elongation due to twinning in a magnesium alloy", *Acta Materialia* **60**, 1433-1443
46. Oppedal, A.L., El Kadiri, H., Tomé, C.N., Kashner, G.C., Voge, S.C., Biard, J.C., Horstemeyer, M.F. (2012), "Effect of dislocation transmutation on modelling hardening mechanisms by twinning in magnesium", *International Journal of Plasticity* **30-31**, 41-61
47. Al-Samman, T., Ahmad, B., Gottstein, G. (2007), "Uniaxial and plane strain compression behaviour of magnesium alloy AZ31: A compression study", *Materials Science forum* **550**, 229-234
48. Larsson, P.L., Giannakopoulos, A.E. (1996), "Analysis of Berkovich indentation", *International Journal of Solid structure* **33**, 221-248
49. Buhagiar, J. (2008), *Plasma surface engineering and characterisation of biomedical stainless steels*, PhD thesis, University of Birmingham, Department of

Metallurgy and Materials, Faculty of Engineering, UK

50. Huang, Y., Zhang, F., Hwang, K.C., Nix, W.D., Pharr, G.M., Feng, G. (2006), "A model of size effects in nano-indentation", *Journal of the Mechanics and Physics of Solids* **54**, 1998-1686
51. Zong, Z., Lou, J., Adewoye, O.O., Elmustafa, A.A., Hammad, F., Soboyejo, W.O. (2006), "Indentation size effects in nano- and micro- hardness of fcc single crystal metals", *Materials Science and Engineering A* **434**, 178-187
52. Gouldstone, A., Chollacoop, N., Dao, M., Li, J., Minor, A.M., Shen, Y. (2007), "Indentation across size scales and disciplines: Recent developments in experimentation and modelling", *Acta materialia* **55**, 4015-4039
53. Jian, J., Zou, J., Sinclair, C.W., Poole, W.J. (2011), "Double tensile twinning in a Mg-8Al-0.5Zn alloy", *Journal of microscopy* **242**, 26-36
54. Korla, R., Chokshi, A.H. (2010), "Strain-rate sensitivity and microstructural evolution in a Mg-Al-Zn alloy", *Scripta Materialia* **63**, 913-916
55. Troyon, M., Huang, L. (2005), "Correction factor for contact area in nanoindentation measurements", *Journal of Materials Research* **20**, 610-617
56. Kang, S., Jung, Y., Yoo, B., Jang, J., Lee, Y. (2012), "Orientation-dependent indentation modulus and yielding in a high Mn twinning-induced plasticity steel", *Materials Science and Engineering A* **532**, 500-504
57. Matsubara, S. (1987), "Application of the Rigid-Triangle vector field to plane-strain wedge indentation into strain-hardening materials", *Annals of the CRIP* **36**,

149-153

58. Johnson, K.L. (1985), *Contact mechanics*. Cambridge University Press

59. Chiu, Y.L., Ngan, A.H.W. (2002), "A TEM investigation on indentation plastic zones in $\text{Ni}_3\text{Al}(\text{Cr},\text{B})$ single crystals", *Acta Materialia* **50**, 2677-269